Gao *et al. Journal of Nanobiotechnology* (2025) 23:339
https://doi.org/10.1186/s12951-025-03382-2

Journal of Nanobiotechnology

RESEARCH Open Access

# Dual-responsive nanoparticles targeting ACE-II senescence for therapeutic mitigation of acute lung injury

Linlin Gao[1†], Fushuang Zheng[2†], Zhiling Fu[3*] and Wei Wang[3*]

**Abstract**

Acute lung injury (ALI) is a life-threatening condition characterized by severe pulmonary dysfunction, with alveolar type II epithelial cell (ACE-II) senescence playing a pivotal role in its progression. In this study, we developed pH/reactive oxygen species (ROS) dual-responsive nanoparticles ($GNP^{santi\text{-}SP\text{-}C}$) for the targeted delivery of Growth Differentiation Factor 15 (GDF15) to counteract ACE-II senescence. These nanoparticles (NPs) effectively activate the AMP-activated protein kinase (AMPK)/Sirtuin 1 (SIRT1) signaling pathway, inducing the mitochondrial unfolded protein response (UPRmt) and reversing senescence-associated cellular dysfunction. $GNP^{santi\text{-}SP\text{-}C}$ were systematically engineered and demonstrated robust pH/ROS sensitivity, efficient GDF15 release, and precise ACE-II targeting. In lipopolysaccharide (LPS)-induced ALI mouse model, $GNP^{santi\text{-}SP\text{-}C}$ treatment significantly mitigated lung injury, reduced inflammatory responses, and enhanced pulmonary function, as evidenced by decreased inflammatory markers, lung edema, and improved histopathology. Single-cell transcriptomic and proteomic analyses revealed increased ACE-II cell populations, reduced expression of senescence markers, and upregulation of AMPK/SIRT1 signaling. In vitro studies further demonstrated that UPRmt activation is associated with the NPs' therapeutic effects, suggesting a potential role in their mechanism of action. These findings demonstrate the potential of GDF15-loaded dual-responsive NPs as an innovative strategy to address cellular senescence and alleviate ALI-associated pulmonary damage.

[†]Linlin Gao and Fushuang Zheng are regarded as co-first authors.

*Correspondence:
Zhiling Fu
20052131@cmu.edu.cn
Wei Wang
20132219@cmu.edu.cn

Full list of author information is available at the end of the article

**Graphical abstract**

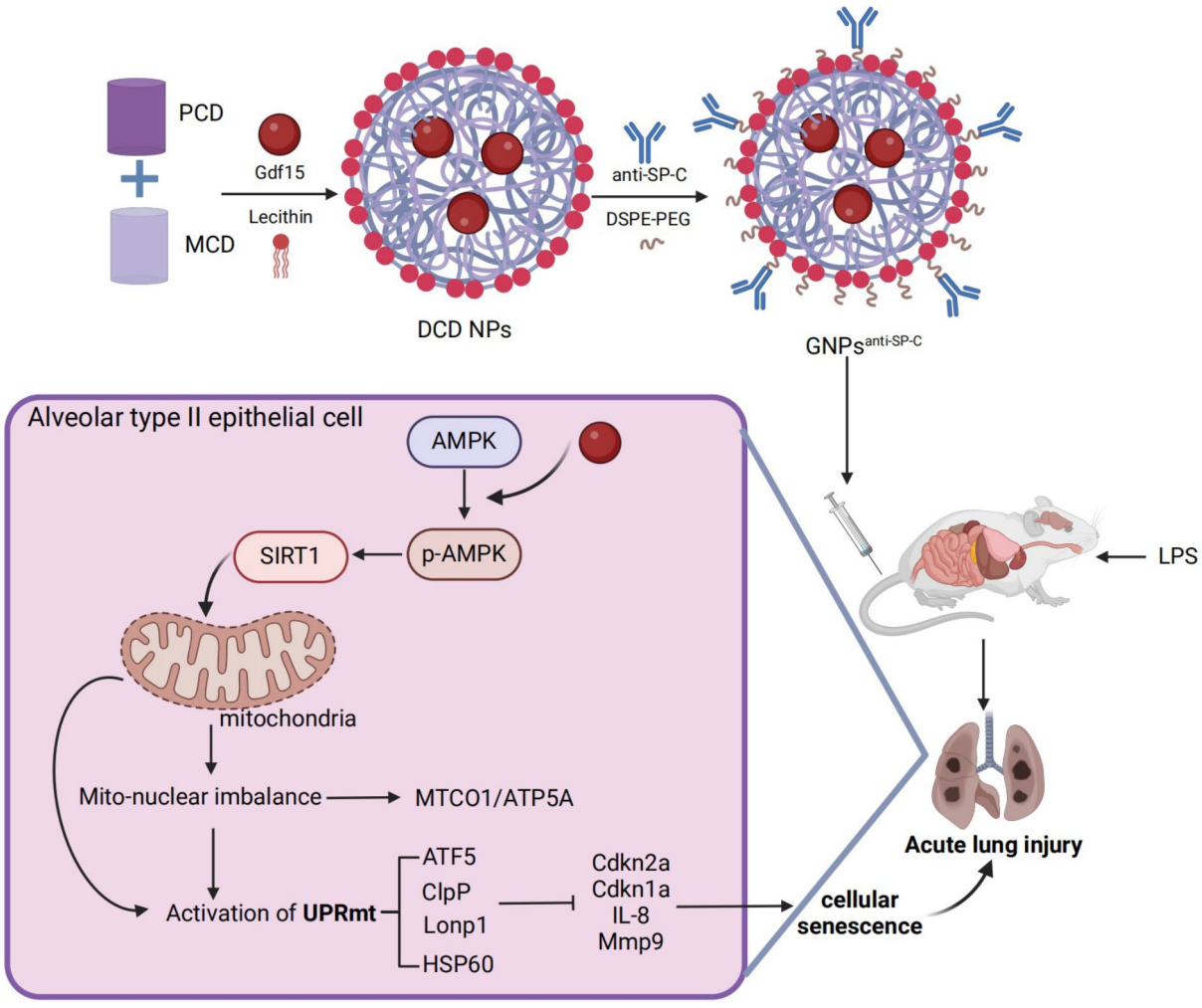


**Keywords** Acute lung injury, Nanoparticle therapy, GDF15, Cellular senescence, AMPK/SIRT1 signaling, Mitochondrial unfolded protein response

## Introduction

Acute lung injury (ALI) is a severe respiratory disease caused by various factors, often characterized by acute inflammatory responses, damage to alveolar epithelial and endothelial cells, and ultimately leading to pulmonary edema, hypoxemia, and respiratory failure [1–3]. The high incidence and mortality of Acute Respiratory Distress Syndrome (ARDS) make it a major global public health issue, especially in intensive care units (ICUs), where its incidence can reach 30–40% [4, 5]. Despite some progress in the pathophysiology and clinical treatment of ALI in recent years, effective therapeutic options for ALI remain limited, primarily relying on supportive therapies such as mechanical ventilation and fluid management, with no specific drugs that can effectively improve patient prognosis [6, 7]. Therefore, in-depth exploration of the pathogenesis of ALI and the identification of new therapeutic targets and strategies is of great scientific and clinical significance [1, 8, 9].

Growth Differentiation Factor 15 (GDF15) is a stress-response factor that is widely expressed in various tissues and cells and plays an important role in cellular stress, inflammatory responses, and metabolic regulation [10–12]. Recent studies have shown that GDF15 has protective effects in various diseases, including cardiovascular diseases, neurodegenerative diseases, and metabolic disorders [13–15]. Specifically, in lung injury, research has found that GDF15 can alleviate lung tissue damage through anti-inflammatory and antioxidant mechanisms and can partially improve the pathological state of ALI

[16, 17]. Moreover, GDF15 has been found to regulate cellular senescence processes by activating intracellular signaling pathways, promoting cell survival, and maintaining cell function [18]. However, the specific mechanisms of GDF15 in ALI, particularly how it alleviates lung injury by regulating cellular senescence, remain underexplored and require further investigation [16, 19].

AMP-activated protein kinase (AMPK) and Sirtuin 1 (SIRT1) are two important intracellular energy metabolism pathways widely involved in energy metabolism, antioxidant stress, inflammatory responses, and cell survival [20]. The AMPK/SIRT1 pathway regulates the activity of various target proteins through phosphorylation and deacetylation, maintaining cellular homeostasis [21–23]. In response to mitochondrial stress, the mitochondrial unfolded protein response (UPRmt) serves as an important cellular protective mechanism by enhancing the folding and degradation capacity of mitochondrial proteins to maintain normal mitochondrial function [24, 25]. Research has shown that the AMPK/SIRT1 pathway plays a critical role in the activation of UPRmt, thereby regulating cellular aging and damage responses. Therefore, studying the role of the AMPK/SIRT1 pathway in ALI, particularly its mechanism of regulating cellular senescence through UPRmt, holds significant scientific value.

In light of the above background, this study aims to explore the molecular mechanism by which pH/reactive oxygen species (ROS) dual-responsive nanoparticles ($GNPs^{anti-SP-C}$) deliver GDF15, activate the AMPK/SIRT1 pathway, and regulate the mitochondrial unfolded protein response (UPRmt) to slow down the senescence of alveolar type II epithelial cells (ACE-II cells) in ALI mice. We first synthesized and characterized pH/ROS-responsive materials and further prepared dual-responsive NPs loaded with GDF15. Through a series of in vitro and in vivo experiments, we validated the targeting, stability, and efficacy of these NPs. The results showed that $GNPs^{anti-SP-C}$ significantly activated the AMPK/SIRT1 pathway, induced UPRmt, reduced ACE-II cell senescence, and improved lung injury in ALI mice. Single-cell transcriptomic sequencing and proteomics analysis further revealed the possible mechanisms of GDF15 in this process. In summary, $GNPs^{anti-SP-C}$ delivering GDF15 through the AMPK/SIRT1 pathway and inducing UPRmt effectively slowed down ACE-II cell senescence and alleviated ALI pathological damage, providing a new strategy and theoretical basis for ALI treatment.

This study not only explores the mechanism of GDF15 in ALI but also uncovers the critical role of the AMPK/SIRT1 pathway. By constructing and optimizing pH/ROS dual-responsive NPs, we achieved efficient delivery of GDF15, significantly improving its stability and targeting in vivo. These findings provide a solid theoretical foundation for the further development of novel therapeutic strategies and are expected to advance the treatment of ALI and other related diseases.

## Materials and methods

### Synthesis of pH-Responsive materials

To modify βcyclodextrin (βCD) with aldehyde functional groups, excess 2-methoxypropylene (MP) was used at room temperature, with pyridinium p-toluene sulfonate (PTS) serving as a catalyst. Specifically, 4 g of βCD was dissolved in 80 mL of anhydrous dimethyl sulfoxide (DMSO), followed by the addition of 64 mg of PTS and 16 mL of MP. After 3 h, about 1 mL of triethylamine was added to terminate the reaction. The resulting aldehyde-modified βCD (MCD) was precipitated from water, collected by centrifugation, and washed four times with deionized water. The remaining moisture was removed by freeze-drying to obtain a white powder.

### Synthesis of ROS-Responsive materials

ROS-responsive βcyclodextrin derivatives (PCD) were chemically functionalized using 4-(hydroxymethyl) phenylboronic acid pinacol ester (PBAP; 702927, Sigma-Aldrich, USA). The specific synthesis steps were as follows: 5.55 g of PBAP (23.6 mmol) was dissolved in 36 mL of anhydrous dichloromethane (DCM; 270997, Sigma-Aldrich, USA), followed by the addition of 7.65 g of 1,1'-carbonyldiimidazole (CDI; 47.2 mmol; 21860, Sigma-Aldrich, USA). After a 30-minute reaction, 40 mL of DCM was added to the mixture, and the resulting solution was washed three times with 30 mL of deionized water. The organic phase was further washed with a saturated NaCl solution, dried over Na2SO4, and concentrated under a vacuum to obtain activated PBAP by CDI. Next, 250 mg of βcyclodextrin (0.22 mmol) and 1.52 g of activated PBAP by CDI (4.62 mmol) were dissolved in 20 mL of anhydrous DMSO, followed by the addition of 0.8 g of 4-dimethylaminopyridine (DMAP; 6.55 mmol; 39405, Sigma-Aldrich, USA). The resulting mixture was stirred magnetically overnight at 20 °C. The final product was precipitated from 80 mL of deionized water, collected by centrifugation, thoroughly washed with deionized water, and collected after freeze-drying.

### Materials characterization

The chemical structure of the synthesized materials was analyzed using hydrogen nuclear magnetic resonance ($^1$H NMR) spectroscopy on an Agilent DD2 600 MHz spectrometer. Fourier-transform infrared (FT-IR) spectra were recorded using a PerkinElmer Spectrum 100 S FT-IR spectrometer to confirm functional group modifications.

### Preparation of GDF15 NPs

To prepare GDF15-loaded nanoparticles (GNPs), 50 mg of the carrier material and 1 mg of Growth Differentiation Factor 15 (GDF15, HY-P77945, MCE, USA) were dissolved in 2 mL of organic solvent to form the organic phase. The aqueous phase was prepared by dispersing 4 mg of phospholipid (P7443, Sigma-Aldrich, USA) and 6 mg of 1,2-distearoyl-sn-glycero-3-phosphoethanolamine-N-[methoxy(polyethylene glycol)-2000] (DSPE-PEG, 880136P, Sigma-Aldrich, USA) in 0.4 mL of ethanol, followed by the addition of 10 mL of deionized water and heating at 65 °C for 1 h. Subsequently, the organic phase was slowly added to the preheated aqueous solution while gently stirring. After vortexing for 3 min, the mixture was cooled to room temperature, incubated for 2 h, and dialyzed with deionized water at 25 °C for 24 h. Finally, the solidified GDF15 protein-loaded NPs (GNPs) were harvested via freeze-drying. DCD NPs were prepared using a 20:80 weight ratio blend of MCD and PCD.

The drug loading content and entrapment efficiency were calculated using the following formulas: Drug loading content (%) = (Weight of GDF15 in NPs / Weight of GDF15-loaded NPs) * 100%; Entrapment efficiency (%) = (GDF15 content in NPs / Theoretical GDF15 content) * 100%.

### Preparation of GNPs targeting ACE-II cells

Initially, the anti-SP-C antibody (ab211326, Abcam, UK) was thiolated at its N-terminus using 2-iminothiolane in PBS (pH = 8.0) and purified by gel filtration through a PD-10 column. Subsequently, the thiolated anti-SP-C antibody (anti-SP-C-SH) was reacted with DSPE-PEG-Mal (880126P, Sigma-Aldrich, USA) in PBS (pH = 6.5) at a protein-to-lipid molar ratio of 1:10 at room temperature for 3 h to obtain anti-SP-C–DSPE-PEG conjugate. The conjugation was achieved by co-incubating the anti-SP-C–DSPE-PEG with GNPs at 37 °C for 1 h to obtain GNPs-anti-SP-C. The molar ratio of GNPs to anti-SP-C antibody was 2000:1.

### Characterization of NPs

The size, particle size distribution, and zeta potential values of various NPs were measured in aqueous solution at 25 °C using a Malvern Zetasizer (Nano ZS90, Malvern Instruments, UK). Transmission electron microscopy (TEM) imaging was conducted using a TECNAI-10 microscope (Philips, The Netherlands) operating at 80 kV acceleration voltage. Scanning electron microscopy (SEM) was carried out on a FIB-SEM microscope (Crossbeam 340, ZEISS), with samples being coated with platinum for 40 s before observation following freeze-drying.

### Hydrolysis of NPs in various solutions

To evaluate the pH and ROS responsiveness of the NPs, hydrolysis tests were conducted in 0.01 M PBS solutions at pH 5, pH 6, or pH 7.4, with or without 1 mM hydrogen peroxide ($H_2O_2$). The solutions containing NPs were incubated at 37 °C for different time intervals, and their transmittance at 500 nm was recorded using UV-visible spectroscopy. Hydrolysis extent was calculated based on changes in transmittance values.

### In vitro drug release profile

To evaluate the pH/ROS dual-responsive drug release profile, freshly prepared DCD NPs loaded with 5 mg of GDF15 protein were incubated at 37 °C in 8 mL of 0.01 M PBS (at pH 5, pH 6, or pH 7.4), with or without 1 mM $H_2O_2$, and agitated at 125 g. At predetermined time intervals, the aqueous solution containing NPs was centrifuged (19118 g), 5.0 mL of the release medium was withdrawn, and an equal volume of fresh medium was replenished. The samples were kept at -20 °C prior to measurement. The cumulative release of GDF15 was quantified using an Enzyme-Linked Immunosorbent Assay (ELISA) kit (MGD150, R&D Systems, USA). The release rates of all GDF15 samples were determined as the average of three replicate measurements.

### Uptake of NPs by mouse lung epithelial cells MLE12

Mouse lung epithelial cells MLE12 were obtained from the American Type Culture Collection (ATCC, CRL-2110, USA) and cultured in Dulbecco's Modified Eagle Medium/Nutrient Mixture F-12 (DMEM/F-12) supplemented with 10% fetal bovine serum (FBS; 26140079, Thermo Fisher Scientific, USA) and 1% penicillin-streptomycin (100 U/mL penicillin and 100 μg/mL streptomycin; 15640055, Thermo Fisher Scientific, USA) in a 5% $CO_2$ humidified atmosphere at 37 °C in an incubator (BB15, Thermo Fisher Scientific, USA).

MLE12 cells were seeded at a density of $2 \times 10^5$ cells per well in 12-well plates. After 24 h, the culture medium was replaced with 1 mL of fresh medium containing 20 μg/mL Cy5-labeled NPs, and the cells were then incubated at 37 °C for specified durations. Prior to observation, the cell nuclei were stained with DAPI. Fluorescent images were captured using an IX53 confocal laser scanning microscope (CLSM; LSM 510 META, Carl Zeiss AG). Likewise, a dose-dependent cellular uptake behavior was examined after 6 h of incubation.

Flow cytometry was used to quantitatively assess NP internalization. MLE12 cells were incubated with 1 mL of fresh medium containing 20 μg/mL Cy5-labeled NPs for various durations or with different doses of Cy5-labeled NPs for 6 h. Subsequently, the cells were digested, and the fluorescence intensity was determined using fluorescence-activated cell sorting (FACS).

### Extracellular cytotoxicity of NPs

MLE12 cells were seeded at a density of $1 \times 10^4$ cells per well in a 96-well plate and allowed to grow for 24 h. After removing the culture medium, the cells were treated with 100 μL of fresh medium containing different concentrations of GDF15-loaded GNPs and GNPs$^{anti-SP-C}$, while cells treated only with fresh medium served as the control. After 24 h, the absorbance of each sample was measured at 450 nm using the Epoch microplate spectrophotometer (Bio-Tek, Winooski, VT, USA). Cell relative viability was calculated based on the control group.

### In vivo biodistribution study of NPs

Male C57BL/6 mice (6–8 weeks old, 18–22 g; Vital River, Beijing, China) were housed in specific pathogen-free (SPF) animal facilities for 1 week prior to the experiment, maintaining constant humidity (45-50%) and temperature (25–27 ℃), with a 12-hour light-dark cycle to acclimate to the experimental conditions. All animal procedures were approved by the Institutional Animal Care and Use Committee.

C57BL/6 mice (3 per group) were intranasally administered with 50 μL of sterile saline, Cy5/GNPs, or Cy5/GNPs$^{anti-SP-C}$ in 50 μL of saline to observe the biodistribution of NPs in the mice. After 2 days of treatment, the mice were euthanized, and their entire viscera were removed. The lungs, heart, spleen, liver, and kidneys were dissected and fixed in 10% formalin. Organ-specific Cy5 fluorescence was detected using the IVIS-200 bioluminescence imaging system (Perkin Elmer, Waltham, MA, USA).

### Immunofluorescence staining

To investigate the colocalization of NPs and ACE-II cell marker ABCA3 in lung tissue, lung tissues treated with physiological saline, Cy5/GNPs, or Cy5/GNPs$^{anti-SP-C}$ physiological saline were dehydrated in 30% sucrose, embedded in O.C.T. (36309ES61, Leica, Shanghai, China), and sectioned into 6 μm frozen sections. The frozen sections were blocked in 3% BSA for 1 h and then incubated overnight with rabbit anti-ABCA3 primary antibody (1:200, ab99856, Abcam, UK). Subsequently, the sections were dual-stained for 1 h in the dark with goat anti-rabbit secondary antibody (Alexa Fluor® 488; 1:1000, ab150077, Abcam, UK).

For the assessment of cellular aging in ACE-II cells in lung tissue, lung tissue sections from each experimental group were prepared as frozen sections and incubated overnight with rabbit anti-ABCA3 (1:200, ab99856, Abcam, UK) or mouse anti-Cdkn2a (1:200, sc-1661, Santa Cruz, USA) primary antibodies. Subsequently, in the dark, the sections were dual-stained for 1 h with goat anti-rabbit secondary antibody (Alexa Fluor® 488) or goat anti-mouse secondary antibody (Cy3®; 1:500, ab97035, Abcam, UK). After washing, the sections were stained with DAPI (1:1000, Beyotime, Shanghai, China) for 10 min, mounted using a mounting medium with antifade reagent (S2100, Solarbio, Beijing, China), and then imaged using CLSM.

### Construction of ALI mouse model

C57BL/6 mice were anesthetized by inhaling 3% isoflurane (792632, Sigma Aldrich, USA). The skin and muscles were sequentially incised to expose the trachea, and a microsyringe was used to slowly inject 100 μL of 1 mg/kg lipopolysaccharide (LPS, L4391, Sigma Aldrich, USA) into the lungs from the distal end of the trachea. Following administration, mice were positioned vertically and gently rocked for 1 min to ensure an even distribution of LPS between the left and right lungs. The successful modeling was confirmed by the presence of moist rales in the lungs, followed by suturing. After 4 h of infection, each mouse was intravenously injected via the tail vein with 1 mg/kg GNPs or GNPs$^{anti-SP-C}$. The administration was repeated every 24 h for a total of 3 doses. At 72 h post-infection, mice were anesthetized with isoflurane inhalation, arterial blood was collected from the descending aorta, and then the mice were euthanized to obtain lung tissue and bronchoalveolar lavage fluid (BALF) for subsequent analysis [26, 27].

Animal experimental groups ($n = 6$ per group): (1) Normal group (treated with physiological saline), Model group (LPS treated), GNPs group (GNPs treatment after LPS infection), and GNPs$^{anti-SP-C}$ group (GNPs$^{anti-SP-C}$ treatment after LPS infection); (2) Model group (LPS treated, Compand C and EX527 solvent control DMSO), GNPs$^{anti-SP-C}$ group (GNPs$^{anti-SP-C}$ treatment after LPS infection, Compand C and EX527 solvent control DMSO), GNPs$^{anti-SP-C}$+Compand C group (GNPs$^{anti-SP-C}$ treatment after LPS infection with intraperitoneal injection of Dorsomorphin (Compand C) 30 min before LPS treatment at a dose of 5 mg/kg [28], and GNPs$^{anti-SP-C}$+EX527 group (GNPs$^{anti-SP-C}$ treatment after LPS infection with intraperitoneal injection of EX527 30 min before LPS treatment at a dose of 5 mg/kg [29]. Compand C (HY-13418 A) and EX527 (HY-15452) were purchased from MCE (USA).

### BALF analysis

To obtain BALF, the lungs were lavaged three times with 1 mL of pre-cooled sterile phosphate-buffered saline (PBS) through the trachea, followed by centrifugation at 1500 g for 5 min at 4 °C. The pelleted cellular sediment was resuspended in 0.5 mL PBS and counted using a hemocytometer after Wright-Giemsa staining. The levels of inflammatory cytokines in the supernatant were analyzed using ELISA.

### ELISA

The total protein concentration in BALF was measured using the BCA Protein Assay Kit (P0012S, Beyotime, Shanghai, China) to assess pulmonary vascular permeability. Additionally, supernatants from cell cultures of each group were collected, and levels of interleukin-1β (IL-1β; PI301, Beyotime, Shanghai, China) and IL-6 (PI326, Beyotime, Shanghai, China) in BALF and cell culture supernatants were measured according to the ELISA kit instructions. The lactate dehydrogenase (LDH) activity in BALF and cell culture supernatants was determined using the LDH assay kit (MAK066-1, Sigma-Aldrich, USA).

Fresh lung tissue homogenates were prepared, and the levels of myeloperoxidase (MPO) in lung tissue were determined using the Mouse MPO ELISA kit (ab155458, Abcam, UK). Absorbance values were measured at 450 nm using a microplate reader (Bio-Tek, Winooski, VT, USA) and analyzed using Origin 9.5 software.

### Hematoxylin and Eosin (H&E) staining

For histological analysis of lung tissues, a portion of the lung was fixed in 4% paraformaldehyde (PFA) for 48 h, embedded in paraffin, and sectioned into 3 μm-thick slices for H&E staining. The sections were first dewaxed and rehydrated through a graded alcohol series. Hematoxylin staining was performed for 2 min, followed by a 10-second rinse in tap water and differentiation in 1% hydrochloric acid ethanol for 10 s. After a 1-minute wash in distilled water, the sections were counterstained with eosin for 1 min, briefly rinsed in distilled water for 10 s, dehydrated through an ascending alcohol series, cleared in xylene, and mounted using a neutral mounting medium.

Tissue morphology was observed under a light microscope (XP-330, Shanghai Bingyu Optical Instrument Co., Ltd., Shanghai, China). Lung injury severity was independently assessed by three pathologists blinded to the experimental groups. Injury was graded based on four key indicators: lung hemorrhage, neutrophil infiltration, pulmonary capillary congestion, and alveolar wall thickening. The severity was classified on a scale of 0 to 4: 0, normal; 1, mild injury (< 25% damage per field); 2, moderate injury (25-50% damage per field); 3, severe injury (50-75% damage per field); 4, very severe injury (> 75% damage per field). The score for each mouse was calculated as the average of five randomly selected areas.

### Pulmonary Wet-to-Dry ratio

Fresh lung tissue was excised, and excess blood was removed before weighing to obtain the wet weight. The samples were then placed in an oven at 80 °C for 24 h until a constant dry weight was achieved. The pulmonary wet-to-dry ratio was calculated as an indicator of lung edema.

### Pulmonary function measurements

Pulmonary function was evaluated using the Buxco Pulmonary Function Testing System (Sharon, Connecticut, CT, USA). Key respiratory parameters, including airway resistance, lung compliance, and pulmonary ventilation, were measured to assess functional lung performance.

### Arterial blood gas analysis

Arterial blood was collected from the descending aorta for the purpose of assessing lung gas exchange and acid-base balance. Oxygen partial pressure ($PaO_2$), carbon dioxide partial pressure ($PaCO_2$), and total carbon dioxide ($TCO_2$) levels were measured using an automated blood gas analyzer.

### Single-Cell transcriptome sequencing (scRNA-seq)

One lung tissue sample from the Model group (untreated) and one from the $GNPs^{anti-SP-C}$ treatment group (treated) of mice were collected. The samples were digested using trypsin (9002-07-7, Sigma-Aldrich, USA) and processed into single-cell suspensions. Individual cells were captured using the C1 Single-Cell Auto Prep System (Fluidigm, Inc., South San Francisco, CA, USA). After cell capture, the cells were lysed within the chip, releasing mRNA, which was then reverse-transcribed to generate cDNA. The lysed and reverse-transcribed cDNA underwent pre-amplification within a microfluidic chip for subsequent sequencing. The amplified cDNA was used for library construction and subjected to single-cell sequencing on the HiSeq 4000 Illumina platform (parameters: paired-end reads, read length 2 × 75 bp, approximately 20,000 reads per cell).

Data analysis was performed using the R software package "Seurat." Data quality control was conducted based on criteria of 200 < nFeature_RNA < 5000 and percent.mt < 20, with a selection of the top 2000 highly variable genes. To reduce the dimensionality of the scRNA-Seq dataset, principal component analysis (PCA) was performed based on the top 2000 highly variable genes. The top 20 principal components were chosen for downstream analysis using the Elbowplot function in the Seurat package. Cell subpopulations were identified using the FindClusters function in Seurat with the default resolution set at res = 1. Subsequently, the UMAP algorithm was applied to perform nonlinear dimensionality reduction on the scRNA-seq sequencing data. Marker genes for various cell subpopulations were selected using the Seurat package, and cell annotations were done by combining known cell lineage-specific marker genes with the online database CellMarker. The "Limma" package in R was used to identify differentially expressed genes in

specific cell subpopulations (AT2 cells) between the two sample groups based on a significance level of $p < 0.05$.

#### Proteomic analysis

Total protein was extracted from lung tissues of untreated ($n = 6$) and treated ($n = 6$) mice, and quantified using the BCA method. Subsequently, after acetone precipitation and trypsin digestion, 100 μg peptide mixtures from each sample were labeled with Tandem Mass Tag (TMT) reagent (A44519, Thermo Fisher Scientific Inc., Waltham, MA, USA). The TMT-labeled peptides were fractionated by reverse-phase (RP) chromatography using an Agilent 1260 Infinity II HPLC system (Agilent Technologies Inc., Santa Clara, CA, USA). Elution was monitored at 214 nm UV trace, collecting fractions every minute from 5 to 50 min, which were then combined into 10 fractions and dried by vacuum centrifugation at 45 °C.

For LC-MS/MS analysis, Orbitrap Exploris 480 mass spectrometer (Thermo Fisher Scientific Inc., Waltham, MA, USA) was utilized, with the raw data processed and quantified using Max Quant software (version 1.5.6.0; Max-Planck-Institute of Biochemistry, Martinsried, Germany). A reverse database search strategy was employed, with a peptide and protein false discovery rate of 1%. Proteins with $|\log2FC| > 1$ and $p$-value $< 0.05$ were considered differentially expressed. Spearman correlation analysis was conducted to investigate the relationship between GDF15 and SIRT1 proteins.

#### GO and KEGG enrichment analysis

In this study, the differential gene expression in AT2 cells obtained from scRNA-seq analysis and the differential proteins identified through proteomic analysis were subjected to Gene Ontology (GO) and Kyoto Encyclopedia of Genes and Genomes (KEGG) enrichment analyses using the "clusterProfiler," "org.Mm.eg.db," "enrichplot," and "ggplot2" packages in R. GO enrichment analysis was carried out for the biological processes (BP), cellular components (CC), and molecular functions (MF), while KEGG enrichment analysis results were visualized using bubble plots and EMAP diagrams. The pairwise similarity of enriched terms was calculated using the Jaccard similarity index (JC), and the results were visualized in EMAP diagrams using the "ggplot2," "igraph," and "ggraph" packages.

#### Isolation of primary ACE-II cells

Primary ACE-II cells were isolated from the lung tissue of C57BL/6 mice. Initially, the lung tissues were perfused with dispase (17105041, Thermo Fisher Scientific, USA) and low-melting-point agarose (A9045, Sigma Aldrich, USA). Subsequently, the tissues were minced and the cell suspension was filtered through a 70 μm cell strainer (431751, Corning, USA) and then passed through a nylon mesh (20 μm pore size). The suspension was centrifuged at 130 g for 8 min at 4 °C. The cells were resuspended in 5 mL of HEPES-buffered DMEM and plated on tissue culture dishes coated with CD45 and CD32 antibodies, followed by a 1-hour incubation at 37 °C with 5% $CO_2$. After centrifugation at 130 g for 8 min, the cells were resuspended in 1 mL of RBC lysis buffer and incubated on ice for 1 min. The cells were then centrifuged at 400 g for 3 min at 4 °C and washed twice with PBS. Subsequently, the cells were resuspended in 250 μL of FACS buffer (PBS + 2% FBS) and incubated with 4 μL of biotinylated anti-EpCAM antibody (13-5791-82, Thermo Fisher Scientific, USA) for cell sorting and purification. Cell purity was evaluated by immunofluorescent staining using antibodies against the ACE-II cell marker Sp-C (1:40, ab211326, Abcam, UK) to assess cell purity (Figure S1).

#### Cell culture and experimental grouping

In the experimental utilization of ACE-II cells, the cells were cultured for 48 h in the ACE-II cell culture medium after seeding. The components of the ATII cell culture medium include DMEM (11966025), 2 mM L-glutamine (25030081), 100 U/mL penicillin and 100 μg/mL streptomycin (15640055), 3.6 mg/mL glucose (A2494001), and 10 mM HEPES (15630130), all purchased from Thermo Fisher Scientific (USA), and supplemented with 10% FBS.

Treated with Compand C (10 μM) [30] or EX527 (5 μM) [31] for 30 min, then induced with 1 μg/mL LPS and further treated with GNPs containing 1 μM GDF15 or $GNPs^{anti\text{-}SP\text{-}C}$ to establish an in vitro model of lung injury cells induced by LPS for 24 h. The specific cell experimental grouping was as follows: (1) Control group (treated with PBS), LPS group, GNPs group (treated with GNPs after LPS infection), and $GNPs^{anti\text{-}SP\text{-}C}$ group (treated with $GNPs^{anti\text{-}SP\text{-}C}$ after LPS infection); (2) LPS group (treated with LPS + Compand C and EX527 solvent control DMSO), $GNPs^{anti\text{-}SP\text{-}C}$ group (treated with $GNPs^{anti\text{-}SP\text{-}C}$ after LPS infection + Compand C and EX527 solvent control DMSO), $GNPs^{anti\text{-}SP\text{-}C}$ + Compand C group (treated with $GNPs^{anti\text{-}SP\text{-}C}$ after LPS infection + Compand C), $GNPs^{anti\text{-}SP\text{-}C}$ + EX527 group (treated with $GNPs^{anti\text{-}SP\text{-}C}$ after LPS infection + EX527).

#### JC-1 staining to assess mitochondrial membrane potential (MMP)

The conventional mitochondrial activity of cells can be evaluated by measuring changes in mitochondrial membrane potential. In a 6-well plate, $1 \times 10^5$ cells were seeded per well and incubated at 37 °C with 5% $CO_2$ for 20–30 min. Then, 2μM JC-1 dye (G1515, Servicebio, China) was added to each well and incubated at 37 °C with 5% $CO_2$ for 15–30 min. Finally, the fluorescence intensity of the cultures (including controls) was

immediately evaluated after replacing the dye with pre-warmed PBS using an Invitrogen EVOS FL imaging system. The ratio of red areas (representing high MMP mitochondria) to green areas (representing total mitochondria) was calculated to evaluate the changes in MMP [32].

#### Flow cytometry to detect cell cycle

Approximately $5.5 \times 10^5$ logarithmic-phase primary ACE-II and MLE12 cells were plated in 6-cm culture dishes with complete medium and allowed to adhere for 16 h, reaching < 30% confluence. Cells were then collected and fixed overnight in 70% ethanol at 4 °C. The fixed cells were washed twice with 1×PBS and stained with 0.5 mL FxCycle PI (propidium iodide)/RNase A staining solution (A10798, Thermo Fisher) for 30 min at room temperature. The cell suspension was analyzed by flow cytometry (BD FACSCelesta), and cell cycle distribution was analyzed using FlowJo software (BD Biosciences) [33].

#### Senescence-Associated βGalactosidase (SA-βGal) activity

According to the manufacturer's instructions, fix the cells at room temperature for 20 min using a fixing solution (PBS solution containing 2% formaldehyde and 0.2% glutaraldehyde). After fixation, rinse the cells twice with PBS, followed by staining the cells with the senescence βgalactosidase staining kit (C0602, Beyotime, Shanghai, China) and incubating at 37 °C for 16 h. Wash the cells three times with PBS, then stain the cell nuclei with DAPI. Mount the coverslip and examine the fluorescence images of SA-βGal-positive cells at a magnification of 200× under an IX53 fluorescent microscope.

#### Reverse transcription quantitative polymerase chain reaction (RT-qPCR)

Total RNA from tissues and cells was extracted using Trizol reagent (15596026, Invitrogen, Thermo Fisher Scientific), and the concentration and purity of the extracted RNA were assessed using a Nanodrop 2000 spectrophotometer (1011U, Nanodrop, Thermo Fisher Scientific, USA). The RNA was reverse transcribed into cDNA following the instructions of the PrimeScript RT Reagent Kit (RR047A, Takara, Japan) at 42 ℃ for 30–50 min and then at 85 ℃ for 5 s. Subsequently, qRT-PCR analysis was performed using the Fast SYBR Green PCR Kit (RR820A, Takara, Japan) and the ABI PRISM 7300 RT-PCR system (Applied Biosystems) with the following cycling conditions: initial denaturation at 95 ℃ for 5 min, followed by 40 cycles of denaturation at 95 ℃ for 30 s, annealing at 57 ℃ for 30 s, and extension at 72 ℃ for 30 s. Three replicates were set up for each sample, with βactin serving as the internal control. The relative gene expression levels were analyzed using the $2^{-\Delta\Delta Ct}$ method, where ΔΔCt = (average Ct value of target gene in experimental group - average Ct value of reference gene in experimental group) - (average Ct value of target gene in control group - average Ct value of reference gene in control group). Each experiment was repeated three times. The primer sequences are listed in Table S1.

#### Western blot

Various cell and tissue samples were collected and lysed in RIPA buffer containing 1% PMSF (P0013B, Beyotime, Shanghai, China) on ice for 30 min at 14,000 g and 4 °C, followed by centrifugation to collect the supernatant. The protein concentration of the samples was determined using the BCA method. Subsequently, 50 μg of denatured protein was loaded after boiling in 5× loading buffer at 100 °C for 10 min. Electrophoresis was performed using separating and concentrating gels, and then the target protein bands were transferred to a PVDF membrane (FFP28, Beyotime, Shanghai, China). The PVDF membrane was blocked with 5% skimmed milk powder for 1 h at room temperature, followed by overnight incubation at 4 °C with primary antibodies against GDF15 (rabbit; 1:5000, 27455-1-AP, Proteintech, Wuhan, China), SIRT1 (rabbit; 1:3000, 13161-1-AP, Proteintech, Wuhan, China), p-AMPK (rabbit; 1:1000, 2535, Cell Signaling Technology, USA), AMPK (rabbit; 1:1000, 2532, Cell Signaling Technology, USA), MTCO1 (rabbit; 1:1000, ab203912, Abcam, UK), ATP5A (rabbit; 1:1000, ab176569, Abcam, UK), ATF5 (rabbit; 1:2000, ab184923, Abcam, UK), ClpP (rabbit; 1:1000, 15698-1-AP, Proteintech, Wuhan, China), Lonp1 (rabbit; 1:1000, 15440-1-AP, Proteintech, Wuhan, China), HSP60 (rabbit; 1:1000, 4870, Cell Signaling Technology, USA), and βactin (rabbit; 1:1000, ab8226, Abcam, UK). After incubation, the membrane was washed with PBST and incubated with HRP-conjugated secondary anti-rabbit IgG (1:10000, BA1054, Bioss, Wuhan, China) at room temperature for 1 h, followed by six washes with PBST for 5 min each. ECL reagent was evenly applied to the membrane, which was then exposed in an Amersham Imager 600 (USA) and analyzed for grayscale using Image J. Each experiment was repeated thrice.

#### Statistical analysis

Statistical analysis of the research data was conducted using GraphPad Prism software (version 9.0, GraphPad Software, San Diego, CA, USA). Descriptive statistics were presented as means ± standard deviations. Initially, normality and homogeneity of variance tests were performed. When the conditions of normal distribution and homogeneity of variance were met, between-group comparisons were carried out using independent t-tests. Multiple group comparisons were conducted through one-way analysis of variance (ANOVA) or repeated measures ANOVA, followed by Tukey's post hoc test. A

significance level of $p < 0.05$ was considered statistically significant.

## Results

### Development of GNPs$^{anti-SP-C}$ for GDF15 loading

To achieve pH responsiveness, we synthesized a pH-responsive material (MCD) through the aldehyde condensation of βCD, and for ROS responsiveness, we combined the oxidation-sensitive PBAP with βCD to obtain a ROS-responsive material (PCD). Characterization through FT-IR and 1 H NMR spectroscopy confirmed the successful synthesis of MCD and PCD (Figure S2A-B). Analysis of the 1 H NMR spectrum of MCD revealed a molar ratio of approximately 0.64 between cyclic and linear aldehydes, corresponding to an aldehyde condensation efficiency of around 88% (Figure S2C). The 1 H NMR spectrum of PCD indicated the presence of approximately 7 PBAP units per βCD molecule (Figure S2D). Subsequently, we employed an improved nano-precipitation/self-assembly method to fabricate different NPs, with phospholipids and DSPE-PEG used for NP stabilization. Successful formation of spherical NPs was confirmed through TEM imaging (Fig. 1A), with a relatively narrow size distribution observed across all NPs (Fig. 1B). All NPs exhibited negative ζ potential (Fig. 1C), with average hydrodynamic diameters ranging from 125 ± 2 to 183 ± 4 nm (Fig. 1D). These results demonstrate the ease of preparation for MCD and PCD NPs, highlighting their favorable compatibility and preparation efficiency.

To demonstrate the pH/ROS dual responsiveness of the NPs, in vitro hydrolysis tests were conducted in PBS containing 1 mM $H_2O_2$ and at different pH values. Significant rapid hydrolysis was observed for MCD NPs at pH 5 or pH 6, with minimal impact from the presence of $H_2O_2$ (Figure S2E). Regardless of the pH value, $H_2O_2$ notably accelerated the hydrolysis of PCD NPs; in contrast, PCD NPs exhibited similar hydrolysis profiles at pH 5, 6, or 7.4 (Figure S2F). The hydrolysis behavior of DCD NPs was influenced by both pH values and $H_2O_2$ (Figure S2G), indicating the excellent pH/ROS dual responsiveness of DCD NPs. Following 6–12 h of incubation in PBS (pH 7.4), DMEM, or 10% serum, no significant changes in the average hydrodynamic diameter were observed for DCD NPs (Fig. 1E), suggesting their good stability in various media.

GDF15 belongs to the transforming growth factor β superfamily and plays a protective role in various inflammatory diseases. Recent studies have shown that GDF15 can prevent LPS-induced ALI, although the specific mechanisms remain unclear [34, 35]. Therefore, we prepared GNPs based on DCD NPs. GNPs exhibited a negative ζ potential and an average hydrodynamic diameter of approximately 123 ± 2 nm (Fig. 1F-G). Further assessment of GDF15 release revealed significantly accelerated release in PBS at pH 5 or pH 6 compared to pH 7.4 (Fig. 1H). The presence of 1 mM $H_2O_2$ greatly enhanced the rate of GDF15 release regardless of the pH variation. These results indicate that GNPs exhibit an excellent pH/ROS dual-responsive drug release capability, aligning with the dual-responsive hydrolysis curves of the corresponding nano-carriers.

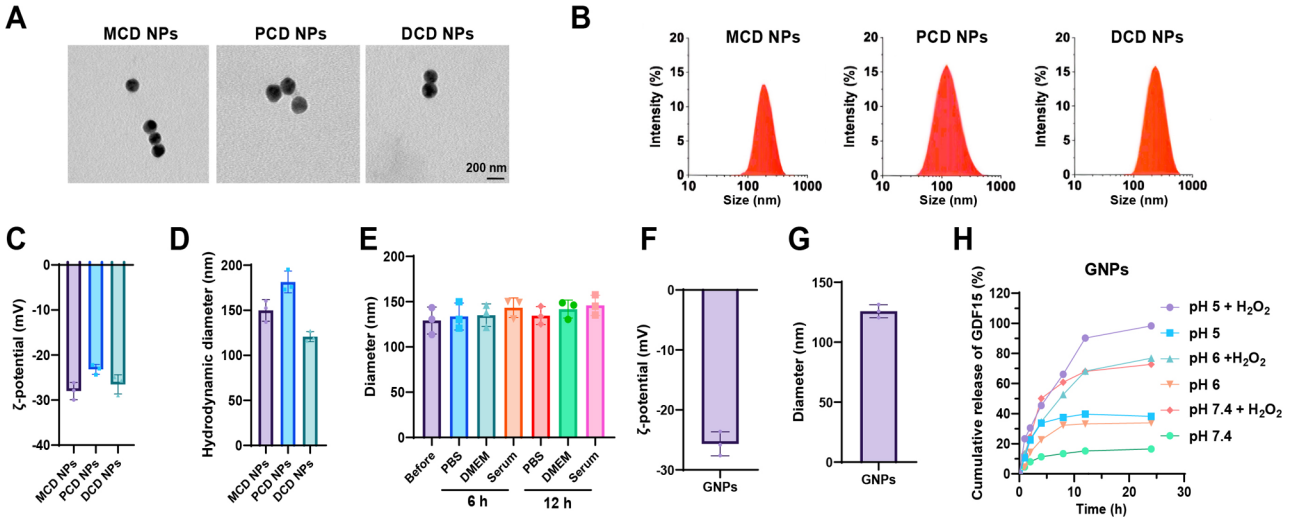


**Fig. 1** Characterization of NPs and Hydrolytic Behavior under Different Conditions. Note: (**A**) TEM images of MCD NPs, PCD NPs, and DCD NPs with scale bars set at 200 nm; (**B**) Size distribution curves of MCD NPs, PCD NPs, and DCD NPs; (**C**) Zeta potential values of MCD NPs, PCD NPs, and DCD NPs; (**D**) Average hydrodynamic diameter of MCD NPs, PCD NPs, and DCD NPs; (**E**) Changes in average hydrodynamic diameter of DCD NPs before and after cultivation in different solutions for varying durations; (**F**) Zeta potential values of GNPs; (**G**) Average hydrodynamic diameter of GNPs; (**H**) In vitro release profiles of GNPs in PBS solutions at pH 5, pH 6, or pH 7.4 (with or without 1 mM $H_2O_2$). Data are presented as mean ± SD, with the experiment repeated 3 times

### GNPs surface modified with Anti-SP-C antibodies exhibit excellent in vitro and in vivo targeting abilities

We conjugated anti-SP-C onto GNPs to obtain GNPs$^{anti-SP-C}$ (Fig. 2A). TEM and SEM observations revealed that GNPs$^{anti-SP-C}$ exhibited a spherical shape with a relatively narrow size distribution; the average hydrodynamic diameter was 132 nm, and the ζ potential was −26.8 ± 0.2 mV (Fig. 2B-D). To validate the targeting ability of GNPs$^{anti-SP-C}$, we first conducted in vitro cellular uptake experiments in mouse lung epithelial cells MLE12 using Cy5-labeled GNPs and GNPs$^{anti-SP-C}$. Confocal microscopy observations and flow cytometry quantitative analysis indicated that the internalization of Cy5/GNPs$^{anti-SP-C}$ in MLE12 cells exhibited clear dose-dependency (Fig. 2E-F) and time-dependency (Fig. 2E-H). Furthermore, the internalization of Cy5/GNPs$^{anti-SP-C}$ in MLE12 cells was significantly increased compared to Cy5/GNPs (Fig. 2I), indicating that the modification with SP-C antibodies enhanced the cellular uptake of NPs by MLE12 cells.

In addition, we evaluated the impact of GNPs and GNPs$^{anti-SP-C}$ at different doses on cell viability, and the

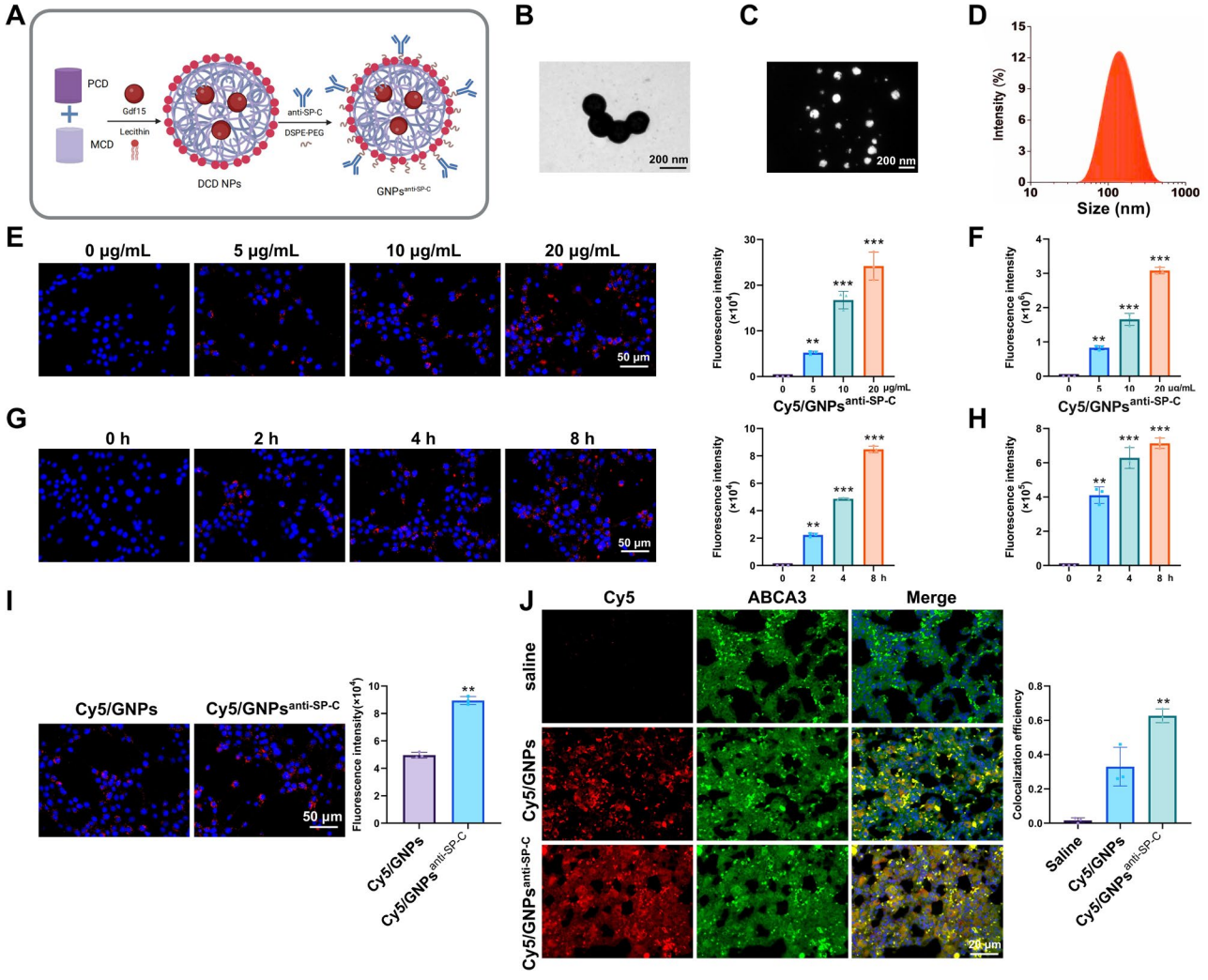


**Fig. 2** Validation of In Vitro and In Vivo Targeting of NPs. Note: (**A**) Schematic illustration of GNPs$^{anti-SP-C}$ synthesis; (**B**-**D**) TEM (**B**), SEM (**C**), and size distribution (**D**) of GNPs$^{anti-SP-C}$, Scale bars = 200 nm; (**E**) Immunofluorescence detection of NPs uptake by MLE12 cells after incubation with different doses of Cy5/GNPs$^{anti-SP-C}$ for 6 h, Scale bars = 50 μm, Cy5: red; DAPI: blue; (**F**) Flow cytometric quantification of NPs internalization by MLE12 cells after incubation with different doses of Cy5/GNPs$^{anti-SP-C}$ for 6 h; (**G**) Immunofluorescence detection of NPs uptake by MLE12 cells after incubation with 20 μg/mL of Cy5/GNPs$^{anti-SP-C}$ for different time periods, Scale bars = 50 μm, Cy5: red; DAPI: blue; (**H**) Flow cytometric quantification of NPs internalization by MLE12 cells after incubation with 20 μg/mL of Cy5/GNPs$^{anti-SP-C}$ for different time periods; (**I**) Immunofluorescence detection of NPs uptake by MLE12 cells after incubation with Cy5/GNPs$^{anti-SP-C}$ and Cy5/GNPs for 6 h, Scale bars = 50 μm, Cy5: red; DAPI: blue; (**J**) Immunofluorescence detection of co-localization of NPs in lung tissue with ACE-II cell marker ABCA3, Scale bars = 20 μm, $n = 3$. Cy5: red; DAPI: blue; ABCA3: green. In panels E-H, ** indicates $p < 0.01$ compared to control (0 μg/mL or 0 h), and *** indicates $p < 0.001$ compared to control (0 μg/mL or 0 h); In panel I, ** indicates $p < 0.01$ compared to Cy5/GNPs; In panel J, ** indicates $p < 0.01$ compared to Cy5/GNPs group. Cell experiments were repeated three times

results showed that NPs loaded with GDF15 exhibited low cytotoxicity, with a significant decrease in cell viability only observed when the GDF15 dose exceeded 1 μM (Figure S3A-B), suggesting that GDF15-loaded NPs had low cytotoxicity at relatively low doses.

Next, the biodistribution of NPs in mice was observed. The relative fluorescence of each organ was measured using the IVIS imaging system. No fluorescence was detected in the lungs, hearts, or spleens of mice treated with saline, while slight spontaneous fluorescence was detected in the kidneys and livers. In contrast, very high levels of fluorescence were detected in the lungs of mice treated with Cy5/GNPs or Cy5/GNPs$^{anti-SP-C}$, with the fluorescence in the lungs of the Cy5/GNPs$^{anti-SP-C}$ group being relatively stronger (Figure S3C). Furthermore, immunofluorescence co-localization analysis revealed no Cy5 fluorescence signal in the lung tissues of the saline-treated group, a significant Cy5 fluorescence signal in the lung tissues of the Cy5/GNPs-treated group with less co-localization signal with the ACE-II cell marker ABCA3, and a significantly enhanced Cy5 fluorescence signal in the lung tissues of the Cy5/GNPs$^{anti-SP-C}$-treated group with a substantial increase in co-localization signal with the AEC2 marker, indicating the uptake of Cy5/GNPs$^{anti-SP-C}$ by ACE-II cells (Fig. 2J).

These results demonstrate that Cy5/GNPs$^{anti-SP-C}$ possess excellent in vitro and in vivo targeting abilities, specifically targeting ACE-II cells.

### The efficacy of GNPs and GNPs$^{anti-SP-C}$ in ameliorating lung injury in ALI mice

We further validated the therapeutic effects of NPs in an ALI mouse model. ALI was induced in mice through LPS administration (Fig. 3A). Histopathological analysis with

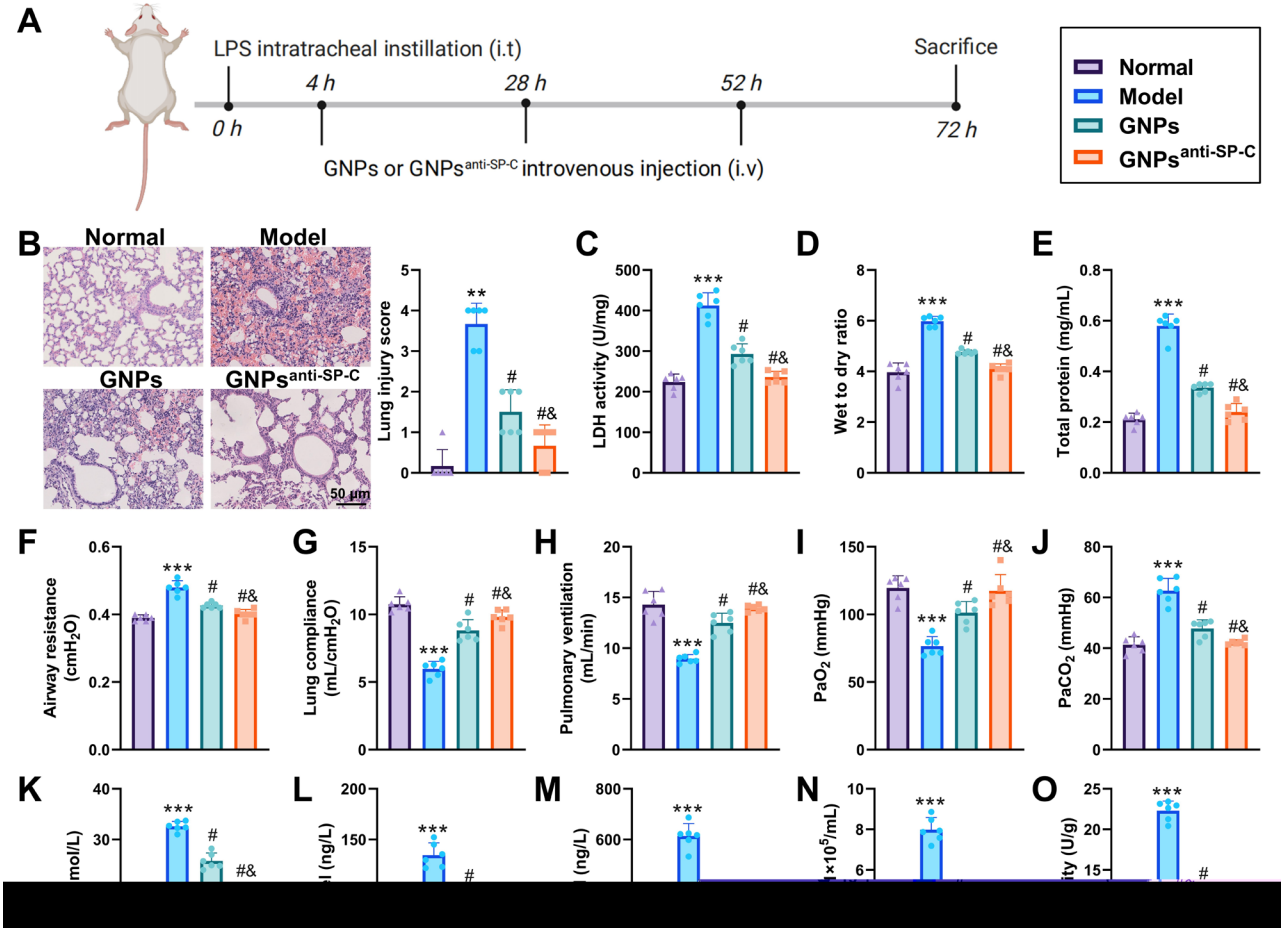


**Fig. 3** GNPs$^{anti-SP-C}$ Regulate ALI Lung Injury in Mice. Note: (**A**) Therapeutic Timeline of ALI Mouse Model; (**B**) Pathological Changes in Lung Tissues of Mice in Each Group Detected by H&E Staining, Scale bars = 50 μm; (**C**) LDH Activity in BALF of Mice in Each Group; (**D**) Lung Wet-to-Dry Weight Ratio of Mice in Each Group; (**E**) Total Protein Concentration in BALF of Mice in Each Group; (**F**-**H**) Evaluation of Lung Function in Mice of Each Group through Airway Resistance (**F**), Lung Compliance (**G**), and Lung Ventilation (**H**); (**I**-**K**) Arterial Blood Gas Analysis Measuring $PaO_2$ (**I**), $PaCO_2$ (**J**), and $TCO_2$ (**K**); (**L**) ELISA Determination of Pro-inflammatory Cytokine IL-1β Levels in BALF of Mice in Each Group; (**M**) ELISA Determination of Pro-inflammatory Cytokine IL-6 Levels in BALF of Mice in Each Group; (**N**) Total Cell Count in BALF of Mice in Each Group; (**O**) Detection of MPO Activity in Lung Tissues of Mice in Each Group by ELISA. ** indicates $p < 0.01$ compared to the Normal group, *** indicates $p < 0.001$ compared to the Normal group, # indicates $p < 0.05$ compared to the Model group, & indicates $p < 0.05$ compared to the GNPs group, with 6 mice in each group

H&E staining revealed significant pathological changes in lung tissues of the Model group, including pulmonary structural damage, thickening of alveolar septa, prominent infiltration of inflammatory cells, and interstitial and alveolar edema. Treatment with GNPs and GNPs$^{anti-SP-C}$ markedly alleviated the LPS-induced lung tissue damage (Fig. 3B). Moreover, GNPs and GNPs$^{anti-SP-C}$ treatment did not cause significant pathological damage to other organs of the mice (heart, liver, spleen, and kidneys) as evidenced in Figure S4. Evaluation of LDH activity showed an increase in the Model group, while GNPs and GNPs$^{anti-SP-C}$ treatment significantly reduced LDH activity (Fig. 3C). Lung edema was assessed by the lung wet-to-dry weight ratio (W/D) and total protein concentration in BALF. Results indicated a significant increase in lung W/D ratio and BALF total protein concentration in the Model group compared to the Normal group, which were significantly reduced in the GNPs and GNPs$^{anti-SP-C}$ groups (Fig. 3D-E). Assessment of lung function through airway resistance, lung compliance, and lung ventilation showed increased airway resistance and decreased lung compliance and ventilation in the Model group. Treatment with GNPs and GNPs$^{anti-SP-C}$ resulted in decreased airway resistance and increased lung compliance and ventilation (Fig. 3F-H). Arterial blood gas analysis revealed decreased $PaO_2$ and increased $PaCO_2$ and $TCO_2$ in the Model group, while GNPs and GNPs$^{anti-SP-C}$ treatment increased $PaO_2$ and decreased $PaCO_2$ and $TCO_2$ (Fig. 3I-K). Notably, the effects of GNPs$^{anti-SP-C}$ in alleviating lung tissue pathology, edema, and respiratory dysfunction were more pronounced compared to GNPs.

In addition, changes in the level of inflammation were assessed. Measurement of the pro-inflammatory cytokines IL-1β and IL-6 levels in BALF showed a significant increase in IL-1β and IL-6 levels in the Model group. Treatment with GNPs and GNPs$^{anti-SP-C}$ led to a significant decrease in IL-1β and IL-6 levels, with GNPs$^{anti-SP-C}$ exhibiting a more pronounced reduction (Fig. 3L-M). Evaluation of MPO activity and total cell count in BALF revealed a significant increase in both parameters in the Model group. Treatment with GNPs and GNPs$^{anti-SP-C}$ resulted in a significant decrease in total cell count and MPO activity, with GNPs$^{anti-SP-C}$ demonstrating a more substantial reduction (Fig. 3N-O).

These results collectively demonstrate that GNPs and GNPs$^{anti-SP-C}$ can improve lung injury in ALI mice, with GNPs$^{anti-SP-C}$ exhibiting superior therapeutic efficacy.

### scRNA-seq analysis reveals the influence of GNPs$^{anti-SP-C}$ on the abundance of AT2 cells in ALI

To further elucidate the specific mechanisms by which GNPs$^{anti-SP-C}$ targets ACE-II (or AT2) cells and improves lung injury, we collected lung tissue from Model (untreated) and GNPs$^{anti-SP-C}$-treated mice for scRNA-seq sequencing analysis. Initially, the data was integrated using the Seurat package. Most cells had a gene count (nFeature_RNA) < 5000, mRNA molecule count (nCount_RNA) < 20,000, and a mitochondrial gene percentage (percent.mt) < 20% (Figure S5A). Subsequently, cells of low quality were removed based on the criteria of 200 < nFeature_RNA < 5000 and percent.mt < 20%, resulting in an expression matrix of 8877 genes and 2657 cells. Correlation analysis of sequencing depth indicated that the filtered data had a correlation coefficient of $r$ = -0.08 between nCount_RNA and percent.mt, and $r$ = 0.93 between nCount_RNA and nFeature_RNA (Figure S5B), indicating good data quality post-filtering and readiness for further analysis.

After analyzing the filtered cells, we identified highly variable genes through variance in gene expression and selected the top 2000 variable genes for downstream analysis (Figure S5C). Cell cycle scoring was performed using the CellCycleScoring function to assess cell cycle status (Figure S5D), followed by data normalization. Next, PCA was conducted on the selected highly variable genes for linear dimension reduction. A heatmap of the major relevant gene expressions for PC_1– PC_6 was presented (Figure S5E), along with the cell distribution in PC_1 and PC_2 (Figure S5F), revealing some batch effects among the samples. Batch correction was performed using the harmony package to enhance cell clustering accuracy (Figure S6A), and the ElbowPlot demonstrated that PCs 1–20 sufficiently represented information from the selected highly variable genes with significant analytical value (Figure S6B). The corrected results indicated effective elimination of batch effects (Figure S6C).

Subsequently, the UMAP algorithm was employed for non-linear dimension reduction on the top 20 principal components, and clustering at different resolutions was displayed using the clustree package (Figure S7). Through UMAP clustering analysis, all cells were categorized into 16 cell clusters (Figure S6D-E). By identifying known cell lineage-specific marker genes from relevant literature and using the CellMarker online tool to find marker genes for various mouse cell types, the cells were annotated, revealing 9 cell types: AT2 cells, Endothelial cells, M1 Macrophages, Lipofibroblasts, Immune cells, Matrix fibroblasts, Brush cells (Tuft cells), B cells, and T cells (Fig. 4A-B). Clusters 0, 5, 7, 8, and 10 were identified as AT2 cells, clusters 1 and 2 as Immune cells, clusters 3 and 13 as Lipofibroblasts, clusters 4 and 6 as Matrix fibroblasts, cluster 9 as Endothelial cells, cluster 11 as Brush cells (Tuft cells), cluster 12 as B cells, cluster 14 as M1 Macrophages, and cluster 15 as T cells. Furthermore, a dot plot illustrating the expression of the 9 cell type-specific marker genes within the cell types was presented (Fig. 4C). Using a T-test, we observed a significant

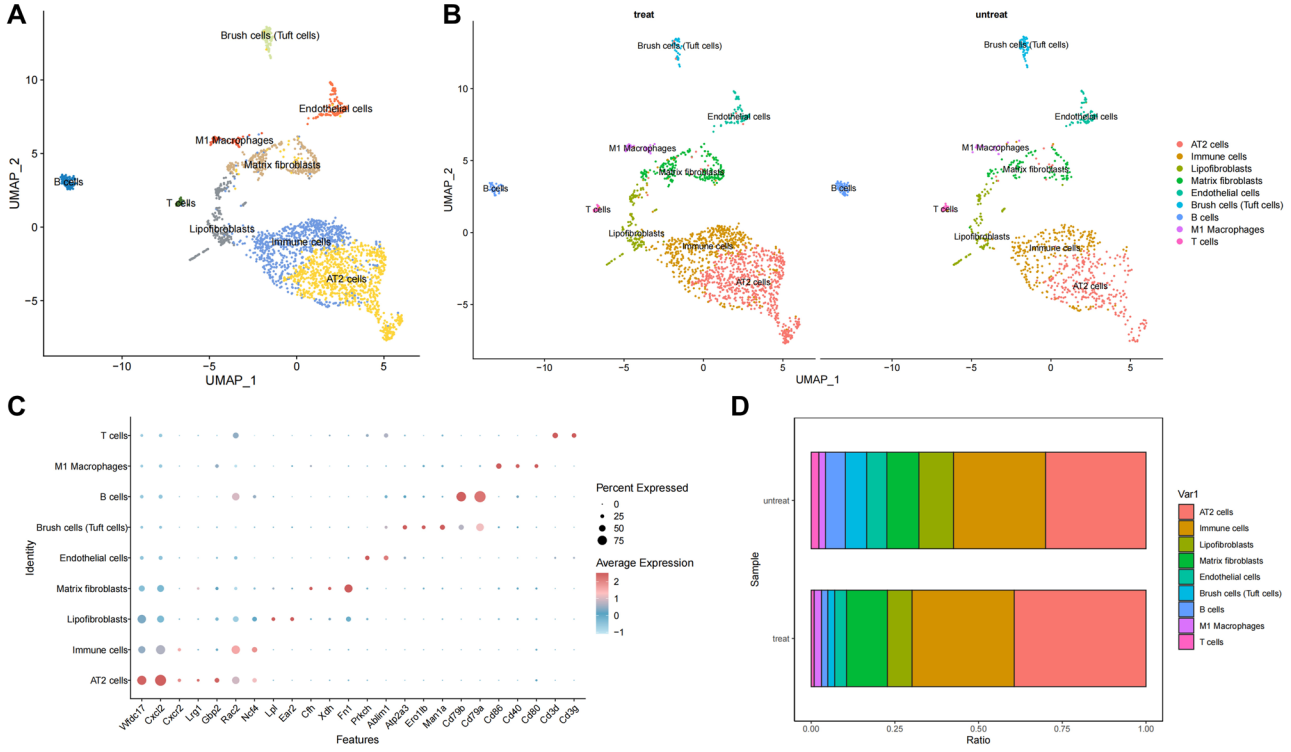


**Fig. 4** scRNA-seq Data Reveals the Impact of NPs Treatment on the Abundance of Various Cell Types in ALI. Note: (**A**) Visualization of cell annotations based on UMAP clustering; (**B**) Grouped visualization of cell annotations based on UMAP clustering; (**C**) Dot plot showing the expression of marker genes for 9 cell types across different cell subgroups, where darker red indicates higher average expression levels; (**D**) Stacked bar chart depicting the proportion of the 9 cell types in each sample group

increase in AT2 cell abundance in the treated group compared to the untreated group (Fig. 4D).

These findings suggest that GNPs$^{anti-SP-C}$ can enhance the abundance of AT2 cells in ALI.

### Single-cell RNA sequencing combined with proteomics reveals that GNPs$^{anti-SP-C}$ delivery of GDF15 May activate the AMPK/SIRT1 pathway involved in ALI cellular senescence process

In this study, we employed scRNA-seq in combination with proteomic analysis to delve into the potential molecular mechanisms of how GNPs$^{anti-SP-C}$ deliver GDF15 in ALI (Fig. 5A). Initially, we performed a differential analysis of AT2 cell marker genes obtained from scRNA-seq, identifying 109 differentially expressed genes (Fig. 5B). Subsequent Gene Ontology (GO) and Kyoto Encyclopedia of Genes and Genomes (KEGG) enrichment analyses of these 109 genes revealed their involvement in cell cytokine-mediated signaling pathways, cellular response to LPS, and other biological processes, exhibiting molecular functions like chemokine receptor binding and NAD binding. Notably, these genes were significantly enriched in NF-kappa B, TNF, cell apoptosis, and cell senescence signaling pathways (Fig. 5C-D).

To further dissect the molecular landscape, we conducted proteomic analysis on lung tissues from the untreated (Model) and GNPs$^{anti-SP-C}$-treated groups, yielding a total of 172 differentially expressed proteins, with 158 upregulated and 14 downregulated proteins (Fig. 5E). The top 50 differentially expressed proteins were subjected to GO and KEGG enrichment analyses, which highlighted their involvement in I-kappaB kinase/NF-kappa B signaling, mitochondrial protein localization, and cellular senescence processes. These proteins act as components of the mitochondrial inner membrane and matrix, exerting molecular functions such as binding to cell cytokine receptors and NAD (Fig. 5F). Moreover, the KEGG analysis demonstrated enrichment in pathways like cytokine-cytokine receptor interaction, TNF signaling, cell apoptosis, cell senescence, and AMPK signaling (Fig. 5G). Collectively, these findings suggest that the delivery of GDF15 by GNPs$^{anti-SP-C}$ may engage in ALI processes associated with inflammatory signaling pathways, cellular senescence, and AMPK-related pathways.

Further construction of the co-expression network for the top 10 differentially expressed proteins revealed that GDF15 and SIRT1 proteins were co-expressed in the treatment group, showing a significant correlation (Fig. 5H). Furthermore, the proteomic differential analysis unveiled that compared to the untreated group, the treated group exhibited notably elevated expression

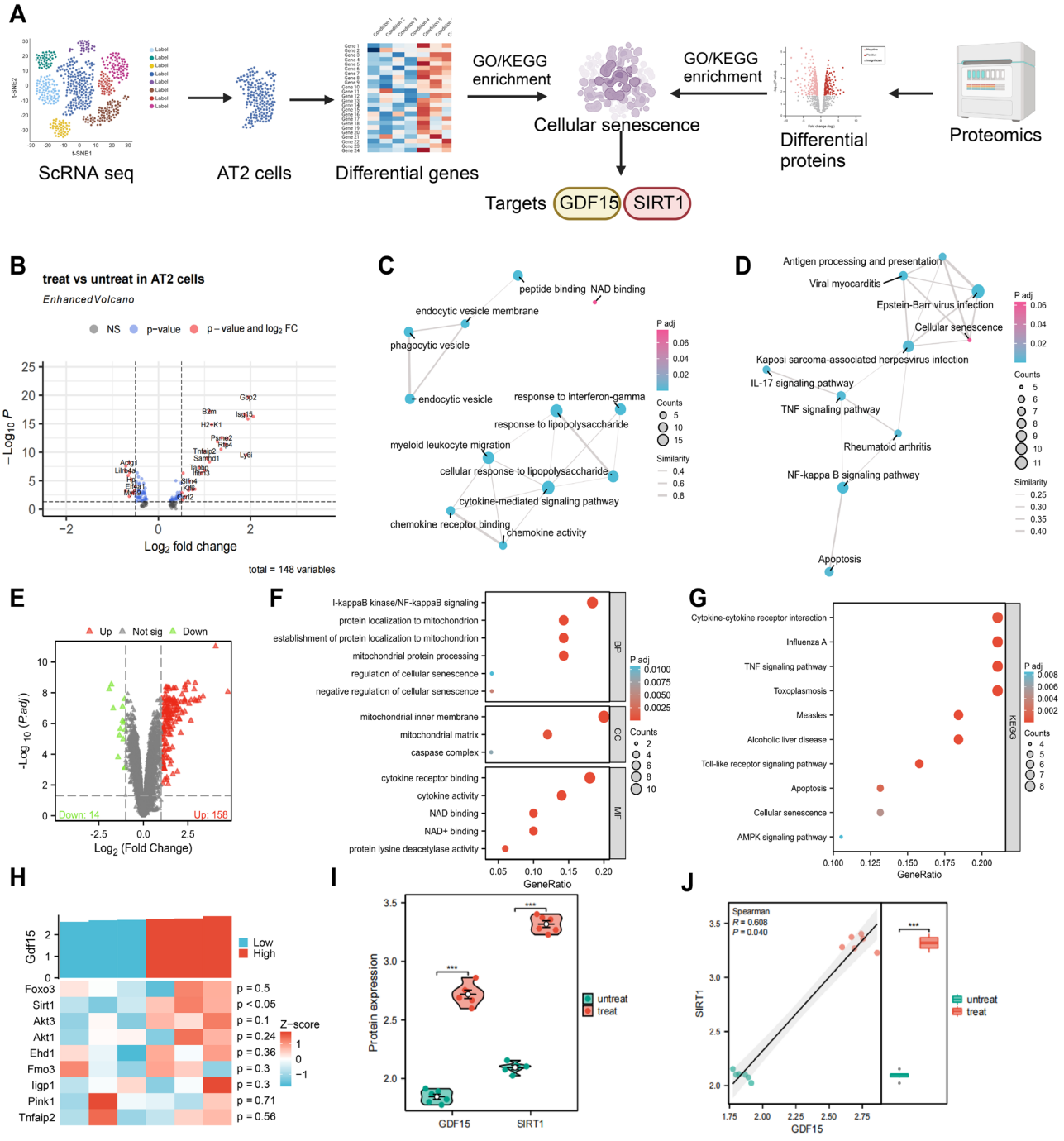


**Fig. 5** scRNA-seq Combined with Proteomics Analysis Reveals the Potential Molecular Mechanism of GDF15 Involvement in ALI. Note: (**A**) The flowchart for screening GDF15 downstream pathways and targets by integrating scRNA-seq with proteomics analysis; (**B**) Volcano plot depicting differentially expressed marker genes in AT2 cells; (**C**-**D**) Enrichment analysis results of differentially expressed marker genes in AT2 cells for Gene Ontology (GO) (**C**) and Kyoto Encyclopedia of Genes and Genomes (KEGG) pathways (**D**). Larger circles represent a higher number of enriched genes, with colors ranging from red to blue indicating decreasing P.adjusted values, and thicker lines denote pairwise similarity where thicker lines signify higher similarity and vice versa; (**E**) Volcano plot showing differentially expressed proteins from proteomic analysis; (**F**-**G**) Enrichment analysis results for the top 50 differentially expressed proteins in AT2 cells for GO (**F**) and KEGG pathways (**G**), where larger circles represent a greater number of enriched genes, and colors from red to blue represent decreasing P.adjusted values; (**H**) Co-expression heatmap of GDF15 and SIRT1 proteins in the treatment group; (**I**) Violin plot depicting the differential expression of GDF15 and SIRT1 proteins in proteomic analysis, *** denotes $p < 0.001$, with 6 untreated and 6 treated samples; (**J**) Scatter plot showing the correlation between the expressions of GDF15 and SIRT1 proteins, *** denotes $p < 0.001$, with 6 untreated and 6 treated samples

levels of GDF15 and SIRT1 proteins (Fig. 5I). Spearman correlation analysis further revealed a significant positive correlation between GDF15 and SIRT1 proteins (Fig. 5J). Existing literature has indicated that GDF15 serves as a biomarker for human cellular senescence and can activate the SIRT1 and AMPK signaling pathways [34, 36, 37]. Drawing upon these bioinformatics analyses, we postulate that GNPs$^{anti-SP-C}$-mediated delivery of GDF15 may engage in the cellular senescence process of ALI by activating the AMPK/SIRT1 pathway.

### GNPs$^{anti-SP-C}$ activation of the AMPK/SIRT1 pathway delays cellular senescence in ALI

Subsequently, we examined the alterations in protein expression of AMPK/SIRT1 signaling pathway proteins and cellular senescence factors during the ALI process and following NPs treatment. Initially, using Western blot analysis, we examined the expression of GDF15 and AMPK/SIRT1 signaling pathway proteins. The results revealed that in the Model group of mice lung tissues, there was a notable increase in GDF15 protein expression (consistent with existing literature [34]), while SIRT1 and p-AMPK protein expressions were significantly reduced, and p-AMPK/AMPK ratio was notably decreased. In contrast, the GNPs and GNPs$^{anti-SP-C}$ groups exhibited significant increases in the expressions of GDF15, SIRT1, and p-AMPK proteins, along with an increase in p-AMPK/AMPK ratio. Notably, the GNPs$^{anti-SP-C}$ group showed a higher expression of SIRT1 and p-AMPK proteins, as well as p-AMPK/AMPK ratio compared to the GNPs group (Fig. 6A-D).

Subsequent analysis involved the examination of senescence markers and the expression of genes associated with senescence-related secretory phenotype (SASP). It was observed that in the Model group of mice lung tissues, mRNA expressions of Cdkn2a, Cdkn1a, IL-8, and Mmp9 were significantly increased. Conversely, both GNPs and GNPs$^{anti-SP-C}$ groups exhibited a significant decrease in the mRNA expressions of these senescence-related genes. Furthermore, the GNPs$^{anti-SP-C}$ group showed a more substantial decrease in the mRNA expressions of these senescence-related genes compared to the GNPs group (Fig. 6E-H). Through immunofluorescence co-localization analysis, it was found that in the Model group, the senescence marker gene Cdkn2a co-localized with the ACE-II cell marker ABCA3. In comparison, the co-localization signals of Cdkn2a and ABCA3 were weakened in both the GNPs and GNPs$^{anti-SP-C}$ groups. Notably, the co-localization signal of Cdkn2a and ABCA3 was significantly weaker in the GNPs$^{anti-SP-C}$ group compared to the GNPs group (Fig. 6I).

Furthermore, in vitro cell models were established through LPS-induced MLE12 cells and primary ACE-II cells to validate the findings. Results indicated a significant increase in LDH activity and levels of pro-inflammatory cytokines IL-1β and IL-6 in the LPS group MLE12 and ACE-II cells. In contrast, both GNPs and GNPs$^{anti-SP-C}$ groups demonstrated a considerable reduction in LDH activity, IL-1β, and IL-6 levels. Additionally, the GNPs$^{anti-SP-C}$ group exhibited significantly lower LDH activity, IL-1β, and IL-6 levels compared to the GNPs group (Fig. 7A-C & Figure S8A-C). Western blot analysis revealed that in the LPS group, GDF15 protein expression was significantly elevated, while SIRT1 and p-AMPK protein expressions were notably decreased, and p-AMPK/AMPK ratio was reduced. Conversely, both GNPs and GNPs$^{anti-SP-C}$ groups displayed significant increases in the expression of GDF15, SIRT1, and p-AMPK proteins, as well as an increase in p-AMPK/AMPK ratio. Interestingly, the GNPs$^{anti-SP-C}$ group exhibited a higher expression of GDF15, SIRT1, and p-AMPK proteins, along with p-AMPK/AMPK ratio compared to the GNPs group (Fig. 7D-G & Figure S8D-G).

The assessment of cellular senescence revealed a significant increase in SA-βgalactosidase-positive cells and mRNA expressions of Cdkn2a, Cdkn1a, IL-8, and Mmp9 in the LPS group. Conversely, both GNPs and GNPs$^{anti-SP-C}$ groups showed a notable decrease in SA-βgalactosidase-positive cells and mRNA expressions of Cdkn2a, Cdkn1a, IL-8, and Mmp9. Furthermore, the GNPs$^{anti-SP-C}$ group exhibited a more substantial reduction in SA-βgalactosidase-positive cells and mRNA expressions of Cdkn2a, Cdkn1a, IL-8, and Mmp9 compared to the GNPs group (Fig. 7H-L & Figure S8H-L).

Cellular senescence has a significant impact on mitochondrial membrane potential. To evaluate the effect of GNPs$^{anti-SP-C}$ on cell mitochondria, we conducted JC-1 staining. The formation of JC-1 aggregates, marked by red fluorescence, indicates the presence of healthy polarized mitochondria. Conversely, JC-1 monomers, indicated by green fluorescence, suggest unhealthy depolarized mitochondria. After incubating the cells with 200 nM JC-1 solution for 20 min, the ratio of red (representing high MMP mitochondria) to green (representing total mitochondria) areas was calculated to assess changes in mitochondrial membrane potential (MMP) in each group. The results showed that after LPS treatment, JC-1 monomers (green) significantly increased, and JC-1 aggregates (red) significantly decreased, indicating a substantial change in mitochondrial depolarization. In contrast, the GNPs and GNPs$^{anti-SP-C}$ groups showed a significant recovery of JC-1 aggregates (red) and a marked decrease in JC-1 monomers (green), suggesting that GNPs and GNPs$^{anti-SP-C}$ could significantly slow down cellular senescence (Fig. 7M & Figure S8M).

To effectively assess the state of cellular senescence, we examined changes in the cell cycle of each group using

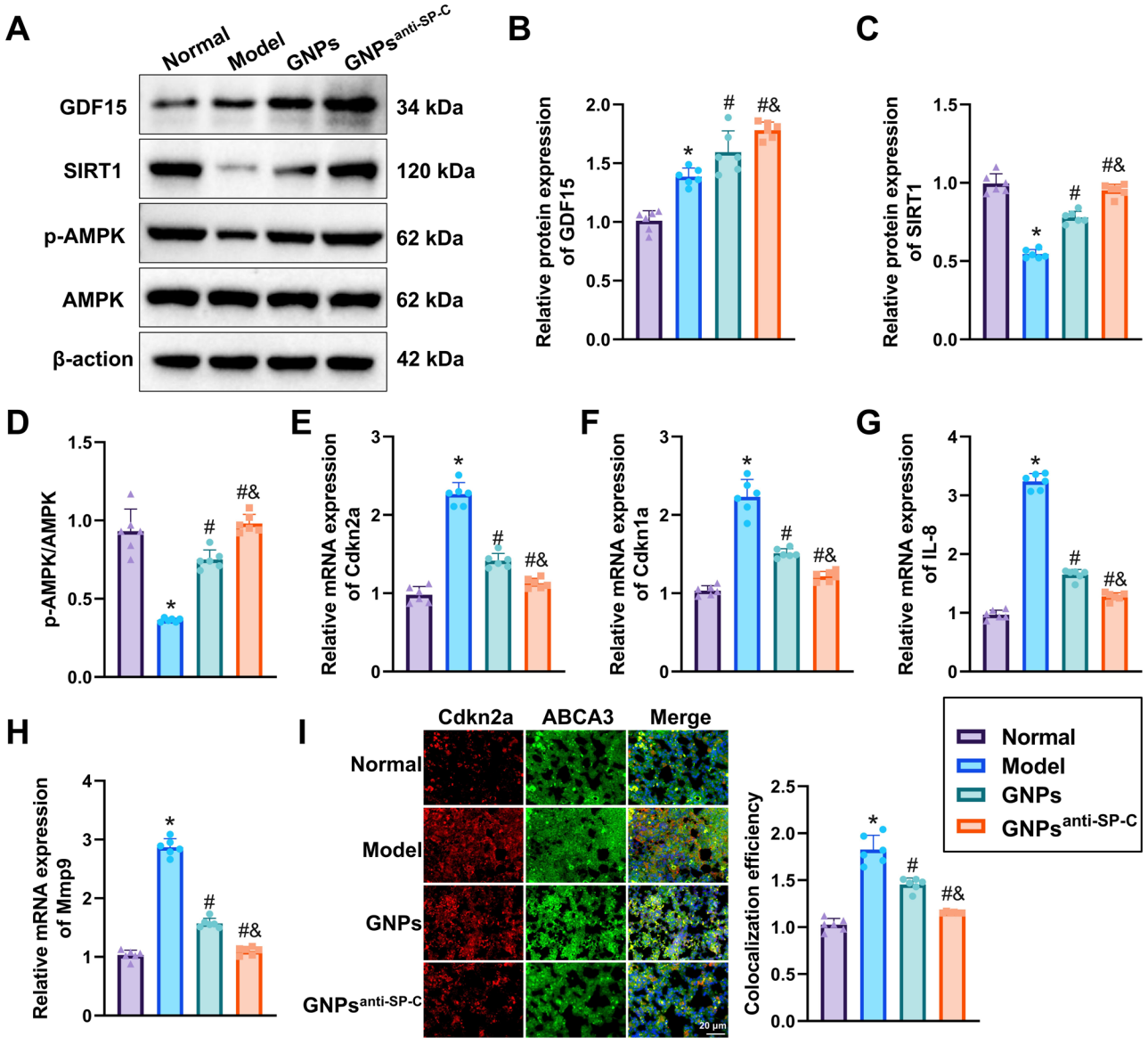


**Fig. 6** Regulation of AMPK/SIRT1 Signaling Pathway Proteins and Cellular Senescence Factors in Lung Tissues of ALI Mice by NPs. Note: (**A**) Western blot detection of GDF15 and AMPK/SIT1 signaling pathway proteins in lung tissues of ALI mice in each group; (**B**-**D**) Protein expression statistics of GDF15 (**B**) and SIRT1 (**C**) in each group, and p-AMPK/AMPK (**D**) statistical graph; (**E**-**H**) RT-qPCR detection of mRNA expression of senescence-related factors Cdkn2a (**E**), Cdkn1a (**F**), IL-8 (**G**), and Mmp9 (**H**) in each group; (**I**) Immunofluorescent colocalization detection of ACE-II cell senescence in lung tissues of each group, where red represents Cdkn2a and green represents ABCA3, Scale bars = 20 μm. Each group consisted of 6 mice. * indicates $p < 0.05$ compared to the Normal group, # indicates $p < 0.05$ compared to the Model group, & indicates $p < 0.05$ compared to the GNPs group

flow cytometry. The results showed that after LPS treatment, the G0/G1 phase cell arrest significantly increased, and the S phase decreased, indicating that LPS treatment induces cellular senescence. In contrast, the GNPs and GNPs$^{anti-SP-C}$ groups showed a marked reduction in G0/G1 phase cell arrest and a significant increase in the S phase, suggesting that these treatments significantly slow down cellular senescence (Fig. 7N & Figure S8N) [33].

These results collectively demonstrate that GNPs$^{anti-SP-C}$ activation of the AMPK/SIRT1 pathway effectively delays cellular senescence in ALI.

### GNPs$^{anti-SP-C}$ induces UPRmt and alleviates LPS-Induced ACE-II cell senescence via activating AMPK/SIRT1 pathway

This study aims to investigate the impact of GNPs$^{anti-SP-C}$ on cellular senescence by modulating the AMPK/SIRT1 pathway. Compand C and EX527 were utilized to inhibit AMPK and SIRT1, respectively. The Western blot analysis revealed that, compared to the LPS group, the GNPs$^{anti-SP-C}$ group exhibited a significant increase in the expression of SIRT1, p-AMPK protein, and the p-AMPK/AMPK ratio. Conversely, in comparison to the GNPs$^{anti-SP-C}$ group, the GNPs$^{anti-SP-C}$+Compand

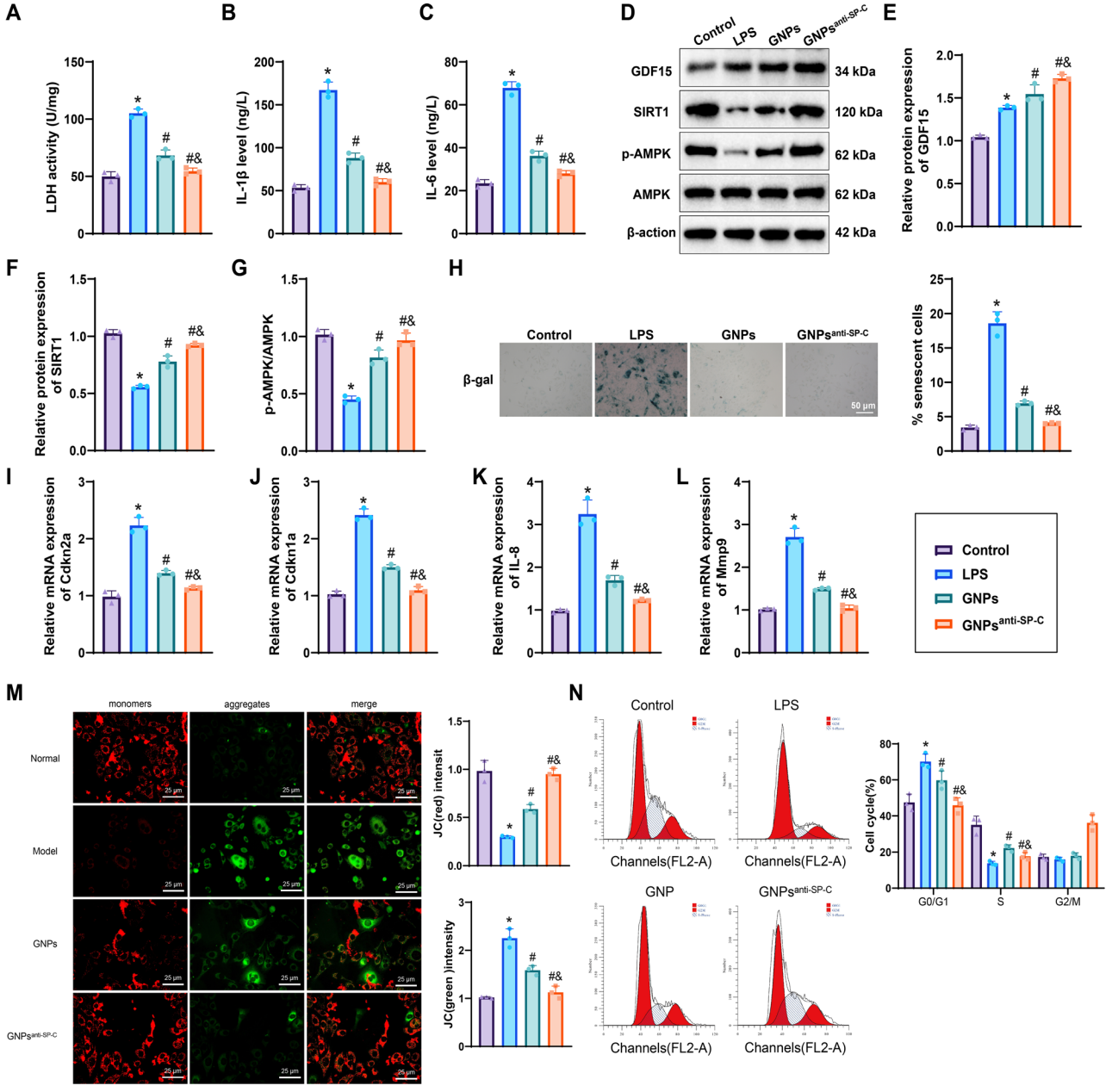


**Fig. 7** Regulation of AMPK/SIRT1 Signaling Pathway Proteins and Cellular Senescence Factors in Primary ACE-II Cells Induced by LPS in the Presence of NPs. Note: (**A**) LDH activity assay in primary ACE-II cells in each group; (**B**-**C**) ELISA detection of IL-1β (**B**) and IL-6 (**C**) levels in the supernatant of each cell group; (**D**) Western blot analysis of GDF15 and AMPK/SIRT1 signaling pathway proteins in primary ACE-II cells in each group; (**E**-**G**) Statistical analysis of GDF15 (**E**) and SIRT1 (**F**) protein expression and p-AMPK/AMPK (**G**) in each group; (**H**) Cellular senescence detection in each group of primary ACE-II cells via SA-βGal staining, Scale bars = 50 μm; (**I**-**L**) RT-qPCR analysis of mRNA expression of senescence-related factors Cdkn2a (**I**), Cdkn1a (**J**), IL-8 (**K**), and Mmp9 (**L**) in each group. (**M**) Measurement of JC-1 levels in each group. JC-1 aggregates (red) indicate normal mitochondrial membrane potential, while JC-1 monomers (green) indicate depolarized mitochondrial membrane potential. (**N**) Measurement of cell cycle changes in each group. Cell experiments were repeated 3 times, * indicates $p < 0.05$ compared to the Control group, # indicates $p < 0.05$ compared to the LPS group, & indicates $p < 0.05$ compared to the GNPs group

C group displayed a notable reduction in SIRT1 expression, p-AMPK protein levels, and p-AMPK/AMPK ratio, while the GNPs$^{anti-SP-C}$+EX527 group showed a decrease in SIRT1 protein expression (Fig. 8A-C & Figure S9A-C).

Analysis of LDH activity and inflammatory cytokine levels in the cells illustrated that, relative to the LPS group, the GNPs$^{anti-SP-C}$ group exhibited a substantial decrease in LDH activity, as well as a significant reduction in pro-inflammatory cytokines IL-1β and IL-6 levels. Moreover, compared to the GNPs$^{anti-SP-C}$ group, both the GNPs$^{anti-SP-C}$+Compand C and GNPs$^{anti-SP-C}$+EX527 groups showed an increase in LDH activity alongside

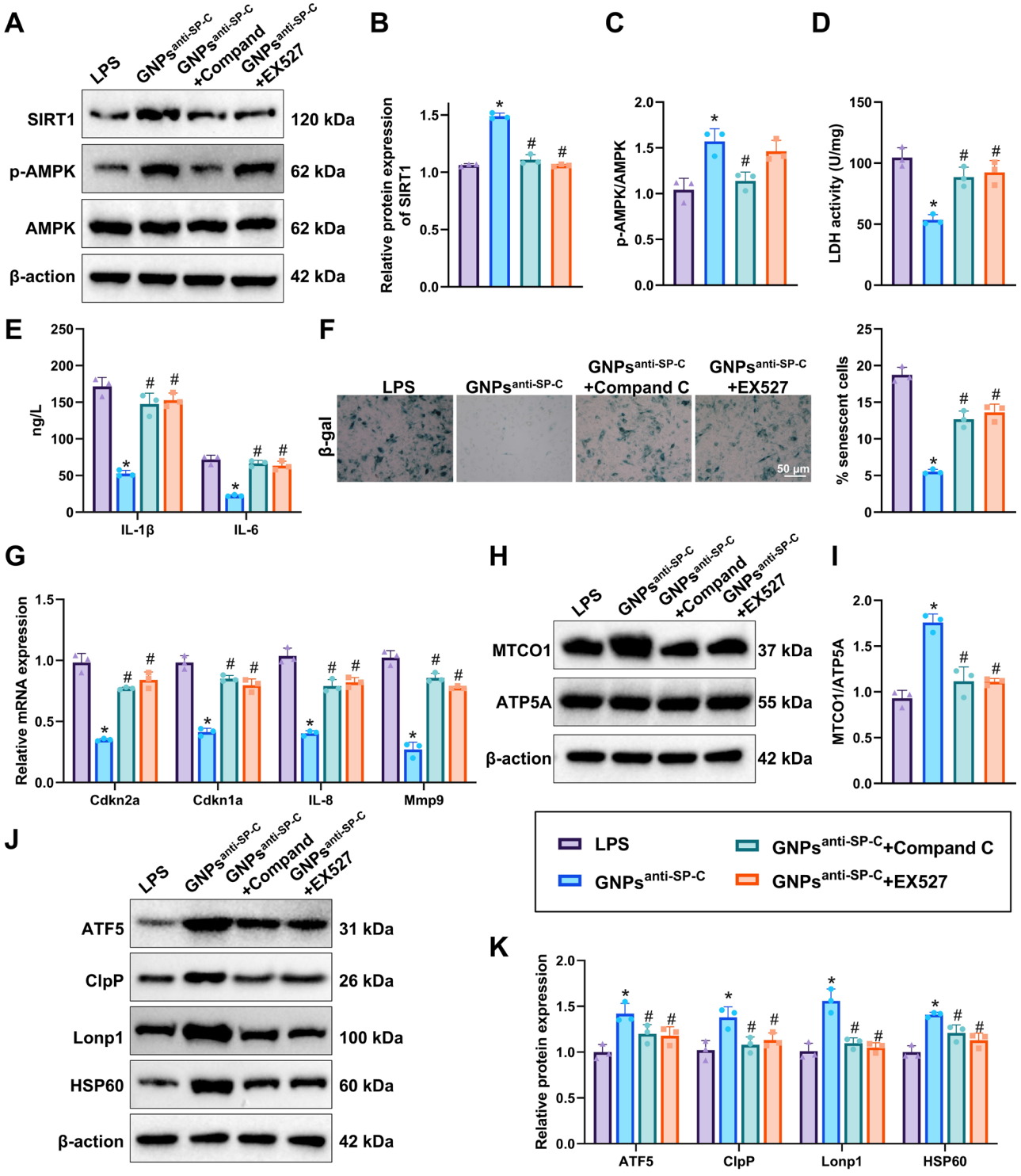


**Fig. 8** The Impact of GNP$^{anti-SP-C}$-induced AMPK/SIRT1 Pathway Regulation on Cellular Senescence in Primary ACE-II Cells. Note: (**A**) Western blot analysis of AMPK/SIRT1 signaling pathway protein expression in primary ACE-II cells in each group; (**B**-**C**) Protein expression of SIRT1 (**B**) and statistical analysis of p-AMPK/AMPK levels (**C**) in each group; (**D**) Measurement of LDH activity in primary ACE-II cells in each group; (**E**) ELISA assessment of IL-1β (**B**) and IL-6 (**C**) levels in cell supernatants in each group; (**F**) Assessment of cellular senescence in primary ACE-II cells in each group using SA-βGal staining, Scale bars = 50 μm; (**G**) RT-qPCR analysis of mRNA expression of senescence-related factors in each group; (**H**-**I**) Western blot analysis of mitochondrial and nuclear protein expression in primary ACE-II cells in each group, as well as statistical analysis of the MTCO1/ATP5A ratio; (**J**-**K**) Western blot analysis of UPRmt-related protein expression in primary ACE-II cells in each group

elevated levels of IL-1β and IL-6 cytokines (Fig. 8D-E & Figure S9D-E). Cell senescence assessment revealed that, in contrast to the LPS group, the GNPs$^{anti-SP-C}$ group displayed a remarkable decrease in SA-βgal positive cells, as well as mRNA expression of Cdkn2a, Cdkn1a, IL-8, and Mmp9. When compared to the GNPs$^{anti-SP-C}$ group, the GNPs$^{anti-SP-C}$+Compand C and GNPs$^{anti-SP-C}$+EX527 groups exhibited a significant increase in SA-βgal positive cells and the mRNA expression of Cdkn2a, Cdkn1a, IL-8, and Mmp9 (Fig. 8F-G & Figure S9F-G).

Mitochondrial dysfunction is a hallmark of cell senescence, with two crucial mechanisms involved: the UPRmt and mitochondrial-nuclear protein imbalance [38]. The imbalance between mitochondrial DNA (mtDNA) and nuclear DNA (nDNA) encoding OXPHOS subunits is termed mitochondrial-nuclear protein imbalance, which is associated with the activation of UPRmt [39]. Therefore, we further examined the changes in UPRmt-related gene protein expressions and mitochondrial-nuclear protein imbalance. Western blot results exhibited a significant increase in the protein expressions of ATF5, ClpP, Lonp1, and HSP60 in the GNPs$^{anti-SP-C}$ group compared to the LPS group, along with an increased ratio between mtDNA-encoded MTCO1 and nDNA-encoded ATP5A. Conversely, compared to the GNPs$^{anti-SP-C}$ group, both the GNPs$^{anti-SP-C}$+Compand C and GNPs$^{anti-SP-C}$+EX527 groups showed a notable decrease in the protein expressions of ATF5, ClpP, Lonp1, and HSP60, with a reduced MTCO1/ATP5A ratio (Fig. 8H-K & Figure S9H-K).

These findings collectively suggest that GNPs$^{anti-SP-C}$ can activate the AMPK/SIRT1 pathway, thereby inducing UPRmt and ameliorating LPS-induced ACE-II cell senescence.

### GNPs$^{anti-SP-C}$ induces mitoprotective effect by activating the AMPK/SIRT1 pathway to attenuate cellular senescence in ALI mice ACE-II cells

In this study, we further investigated the mechanism by which GNPs$^{anti-SP-C}$ alleviates cellular senescence in ALI mouse models. Histological analysis through H&E staining revealed that treatment with GNPs$^{anti-SP-C}$ significantly alleviated lung tissue damage induced by LPS, while mice in the GNPs$^{anti-SP-C}$+Compound C and GNPs$^{anti-SP-C}$+EX527 groups exhibited increased lung injury compared to the GNPs$^{anti-SP-C}$ group (Figure S10A). Evaluation of LDH activity showed a significant reduction in LDH levels with GNPs$^{anti-SP-C}$ treatment, whereas the GNPs$^{anti-SP-C}$+Compound C and GNPs$^{anti-SP-C}$+EX527 groups had elevated LDH activity compared to the GNPs$^{anti-SP-C}$ group (Figure S10B). Moreover, the lung W/D ratio and total protein concentration in the BALF were significantly decreased in the GNPs$^{anti-SP-C}$ group compared to the GNPs$^{anti-SP-C}$+Compound C and GNPs$^{anti-SP-C}$+EX527 groups, indicating exacerbated lung injury in the latter (Figure S10C-D). Assessment of lung function parameters including airway resistance, lung compliance, and ventilation revealed that the GNPs$^{anti-SP-C}$ group had decreased airway resistance and increased lung compliance and ventilation compared to the GNPs$^{anti-SP-C}$+Compound C and GNPs$^{anti-SP-C}$+EX527 groups, which exhibited the opposite trend (Figure S10E-G). Arterial blood gas analysis demonstrated an increase in $PaO_2$ and a decrease in $PaCO_2$ and $TCO_2$ in the GNPs$^{anti-SP-C}$ group, while the GNPs$^{anti-SP-C}$+Compound C and GNPs$^{anti-SP-C}$+EX527 groups showed reduced $PaO_2$ and elevated $PaCO_2$ and $TCO_2$ levels compared to the GNPs$^{anti-SP-C}$ group (Figure S10H-J).

Furthermore, a significant decrease in inflammation levels was observed in the GNPs$^{anti-SP-C}$ group, as evidenced by markedly reduced levels of IL-1β and IL-6, total cell count, and MPO activity in the BALF. In contrast, the GNPs$^{anti-SP-C}$+Compound C and GNPs$^{anti-SP-C}$+EX527 groups exhibited a significant increase in IL-1β and IL-6 levels, total cell count, and MPO activity compared to the GNPs$^{anti-SP-C}$ group (Figure S10K-N). These findings suggest that inhibition of the AMPK/SIRT1 signaling pathway attenuates the protective effect of GNPs$^{anti-SP-C}$ against ALI in mice.

Western blot analysis demonstrated a significant increase in SIRT1 expression, p-AMPK protein levels, and p-AMPK/AMPK ratio in the GNPs$^{anti-SP-C}$ group compared to the Model group. Conversely, the GNPs$^{anti-SP-C}$+Compound C group showed reduced SIRT1 expression, p-AMPK protein levels, and p-AMPK/AMPK ratio relative to the GNPs$^{anti-SP-C}$ group, while the GNPs$^{anti-SP-C}$+EX527 group exhibited decreased SIRT1 protein expression (Fig. 9A-C).

Analysis of cellular senescence revealed that mRNA expression levels of Cdkn2a, Cdkn1a, IL-8, and Mmp9 were significantly decreased in the GNPs$^{anti-SP-C}$ group compared to the Model group. However, the GNPs$^{anti-SP-C}$+Compound C and GNPs$^{anti-SP-C}$+EX527 groups showed a notable increase in the expression of these genes relative to the GNPs$^{anti-SP-C}$ group (Fig. 9D). Immunofluorescence co-localization analysis demonstrated a reduction in co-localization signals between the senescence marker gene Cdkn2a and ACE-II cell marker ABCA3 in the GNPs$^{anti-SP-C}$ group compared to the Model group. Conversely, the GNPs$^{anti-SP-C}$+Compound C and GNPs$^{anti-SP-C}$+EX527 groups exhibited enhanced co-localization signals between Cdkn2a and ABCA3 compared to the GNPs$^{anti-SP-C}$ group (Fig. 9E).

Previous studies have found that CTRP3 can activate the UPRmt signaling pathway through the SIRT1/ATF5 axis to alleviate mitochondrial dysfunction and oxidative stress in pathological cardiac hypertrophy [40]. However,

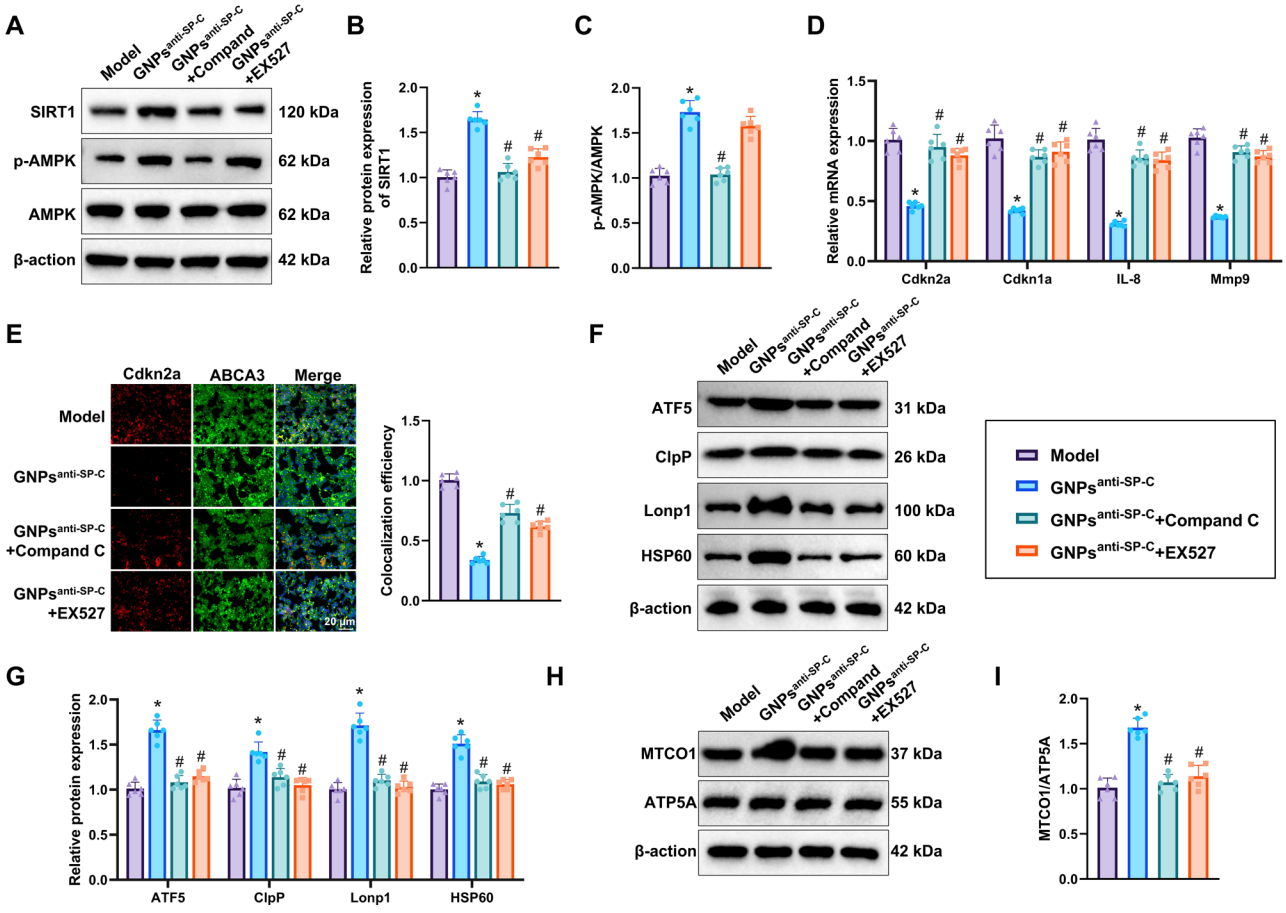


**Fig. 9** The Impact of GNPs$^{anti-SP-C}$ on the AMPK/SIRT1 Pathway Regulation of Cell Senescence in ALI Mice. Note: (**A**) Expression of AMPK/SIRT1 pathway proteins in mouse lung tissues of each group was detected by Western blot; (**B**-**C**) Protein expression of SIRT1 (**B**) and statistical graph of p-AMPK/AMPK ratio (**C**) in each group; (**D**) mRNA expression of senescence-related factors in each group was measured by RT-qPCR; (**E**) Immunofluorescence co-localization detection of ACE-II cells senescence in mouse lung tissues of each group, where red represents Cdkn2a and green represents ABCA3. Scale bars = 20 μm; (**F**-**G**) Expression of UPRmt-related proteins in MLE12 cells of each group was assessed by Western blot; (**H**-**I**) Expression of mitochondrial and nuclear proteins in MLE12 cells of each group was examined by Western blot, and statistical graph of MTCO1/ATP5A ratio. * denotes $p < 0.05$ compared to the Model group, and # denotes $p < 0.05$ compared to the GNPs$^{anti-SP-C}$ group, with 6 mice per group

there have been no studies linking GNPs$^{anti-SP-C}$'s effects on UPRmt via the AMPK/SIRT1 pathway. Therefore, we further assessed the expression of UPRmt-related proteins ATF5, ClpP, Lonp1, and HSP60 was significantly increased in the GNPs$^{anti-SP-C}$ group compared to the Model group. The ratio of MTCO1 encoded by mtDNA to ATP5A encoded by nDNA also increased. However, the GNPs$^{anti-SP-C}$+Compound C and GNPs$^{anti-SP-C}$+EX527 groups showed a significant decrease in the expression of ATF5, ClpP, Lonp1, and HSP60, along with a reduction in the MTCO1/ATP5A ratio compared to the GNPs$^{anti-SP-C}$ group (Fig. 9F-I).

These results indicate that GNPs$^{anti-SP-C}$ can activate the AMPK/SIRT1 pathway to induce UPRmt and attenuate ACE-II cell senescence, thereby alleviating ALI in mice.

## Discussion

This study demonstrates that GNPs$^{anti-SP-C}$ can deliver GDF15 to activate the AMPK/SIRT1 pathway, induce UPRmt, and significantly attenuate ALI in mice by reducing senescence in ACE-II, thereby improving lung damage. Compared to previous studies, this research systematically reveals for the first time the protective mechanism of GDF15 in ALI, particularly its regulatory role in UPRmt through the AMPK/SIRT1 pathway. Additionally, this study employs an innovative pH/ROS-responsive nanoparticle technology to achieve precise targeting and efficient release of GDF15, overcoming limitations of traditional drug delivery methods and offering a new strategy for ALI treatment.

GDF15, as a stress-responsive factor, exhibits significant protective effects in various pathological conditions

[41, 42]. Previous studies have shown that GDF15 can alleviate lung tissue damage and improve the pathological state of ALI through anti-inflammatory and antioxidant mechanisms [43]. However, the short half-life and uneven distribution of GDF15 in vivo have restricted its clinical effectiveness [44, 45]. This study significantly enhances the stability and targeting of GDF15 in vivo by delivering it via NPs, thereby enhancing its therapeutic efficacy. Our results demonstrate that GNPs$^{anti-SP-C}$ not only efficiently delivers GDF15 but also enhances its biological function by activating the AMPK/SIRT1 pathway, thereby significantly reducing senescence in ACE-II cells and ALI pathology.

The AMPK/SIRT1 pathway plays a crucial role in cellular energy metabolism and antioxidant stress. Previous studies have indicated that activation of the AMPK/SIRT1 pathway can enhance cellular stress resistance, promote cell survival, and maintain functionality. In this study, we found that GDF15 significantly enhances UPRmt activity and alleviates LPS-induced senescence in ACE-II cells by activating the AMPK/SIRT1 pathway. This discovery reveals, for the first time, the key role of the AMPK/SIRT1 pathway in GDF15-mediated UPRmt regulation, expanding our understanding of the involvement of the AMPK/SIRT1 pathway in cellular protection.

Nanoparticle technology has emerged as a promising drug delivery system, with widespread applications in targeted delivery and controlled release therapies [46]. Compared to traditional drug delivery methods, NPs offer advantages such as small particle size, large surface area, high drug loading capacity, and good biocompatibility [47, 48]. In this study, GNPs$^{anti-SP-C}$ were utilized to achieve precise drug release in the pathological environment of ALI, enhancing therapeutic efficacy while reducing side effects. Characterization and in vitro/in vivo experiments confirmed the excellent targeting and drug release properties of these NPs, laying the groundwork for future therapeutic research.

The UPRmt serves as a crucial cellular protective mechanism, playing a key role in maintaining mitochondrial function and cellular homeostasis [49, 50]. Prior studies have shown that UPRmt alleviates cellular stress and damage by enhancing the folding and degradation capacity of mitochondrial proteins [51, 52]. In this study, we discovered that through activation of the AMPK/SIRT1 pathway, GDF15 significantly enhanced UPRmt activity, mitigating cellular senescence and ALI pathological damage in ACE-II cells. The AMPK/SIRT1 pathway helps repair damaged mitochondria and restores their normal function. This not only reduces cellular stress caused by mitochondrial dysfunction but also enhances cellular energy metabolism efficiency. Furthermore, through these mechanisms, the AMPK/SIRT1 pathway and UPRmt together likely reduce the accumulation of ROS within cells, decreasing oxidative stress damage and thus slowing cellular senescence. Therefore, by repairing damaged mitochondria and reducing cellular senescence, the AMPK/SIRT1 pathway and UPRmt cooperate to improve the function of type II alveolar epithelial cells (ACE-II cells), enhancing lung compliance and ventilation capacity, and alleviating ALI symptoms. This finding supports the potential of UPRmt as a cellular protective target, offering new insights for ALI treatment.

In our study, the effectiveness of GNPs$^{anti-SP-C}$ in ALI treatment was systematically evaluated through in vivo and in vitro experiments. The results demonstrated that GNPs$^{anti-SP-C}$ significantly reduced lung injury in mice, improved lung function, decreased inflammatory responses, and cellular aging. These findings not only validate the potential of nanoparticle technology in ALI treatment but also provide crucial experimental evidence for future clinical translation studies. However, issues concerning the safety, efficacy, and large-scale production of NPs still require further investigation and optimization.

By synthesizing GNPs$^{anti-SP-C}$ in this study, precise delivery and efficient release of GDF15 were achieved, revealing the induction of UPRmt through activation of the AMPK/SIRT1 pathway, thereby slowing down ACE-II cell aging and alleviating ALI pathology. Our research results hold significant scientific importance and offer new strategies and theoretical basis for the clinical treatment of ALI. Nonetheless, the study has certain limitations, such as a limited sample size and potential risks associated with long-term nanoparticle exposure in vivo. Future research should focus on optimizing nanoparticle design, validating their effectiveness and safety in large animal models, and exploring their potential applications in other inflammatory lung diseases.

## Conclusion

Based on the aforementioned results, we can preliminarily draw the following conclusions: the GNPs$^{anti-SP-C}$ that we developed for targeting ACE-II cells can deliver GDF15, activate the AMPK/SIRT1 pathway, induce UPRmt, attenuate cellular senescence in ACE-II cells, thereby alleviating lung injury in mice (Fig. 10). The synthesis of pH/ROS dual-responsive NPs (GNPs$^{anti-SP-C}$), targeting ACE-II cells, has enhanced the targeted therapy effectiveness against ALI, making GNPs$^{anti-SP-C}$ a promising novel nanomedicine for treating ALI. Nonetheless, our study has certain limitations. Firstly, the disparity between in vitro and in vivo models may impact the actual application effectiveness of the NPs, necessitating further validation of their efficacy and safety in different animal models and humans. Secondly, this study primarily focuses on short-term effects, without evaluating the potential toxicity and immune response associated with

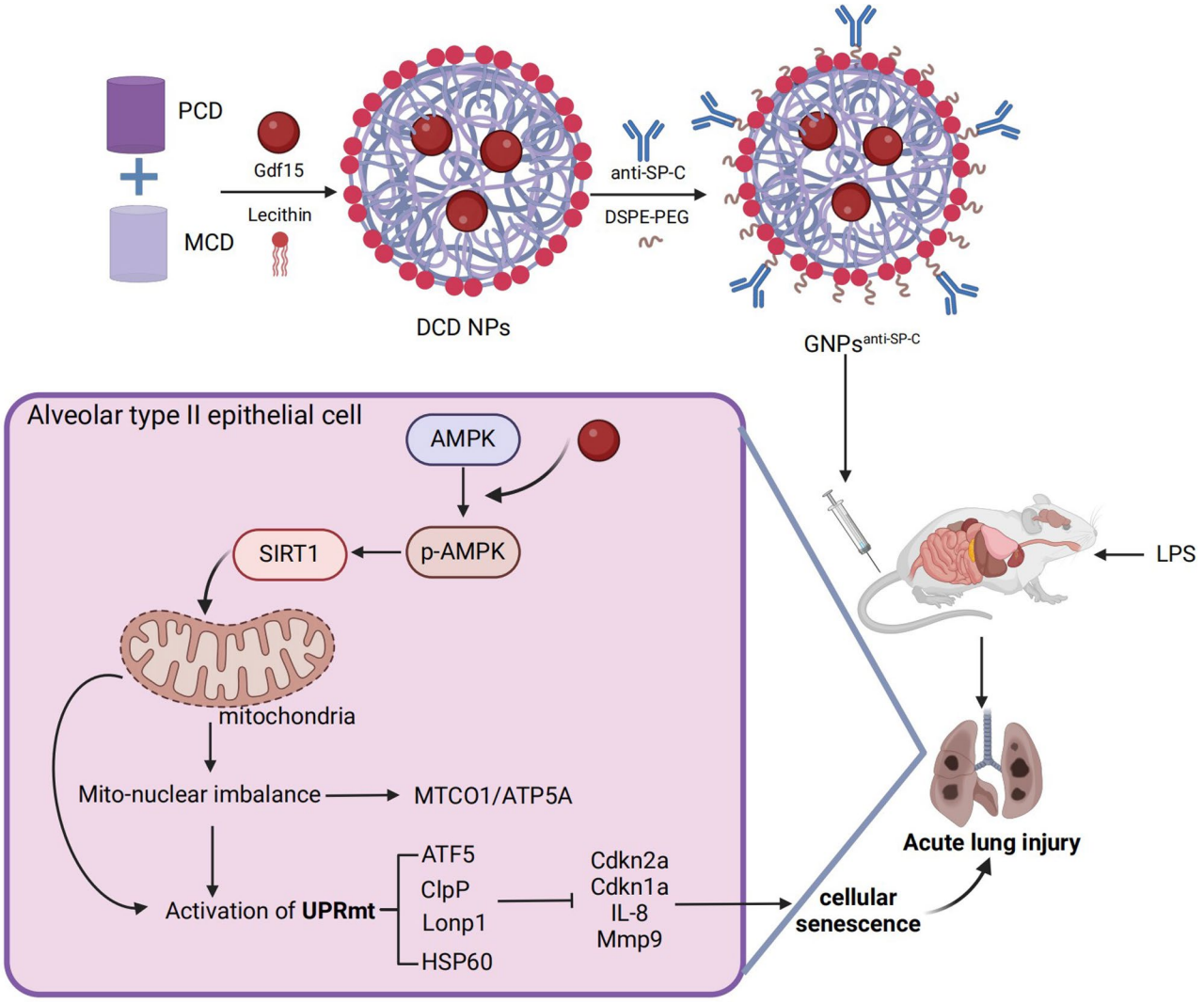


**Fig. 10** Molecular Mechanism Schematic of GDF15 Delivered by GNPs$^{anti-SP-C}$ Mediating the Regulation of UPRmt via the AMPK/SIRT1 Pathway Affecting ACE-II Cell Senescence in ALI Mice

long-term nanoparticle use. Subsequently, we will conduct additional research on the chronic toxicity of NPs and explore their application in various animal models to provide more theoretical foundations and insights for using GNPs$^{anti-SP-C}$ in clinical ALI treatment.

## Supplementary Information

The online version contains supplementary material available at https://doi.org/10.1186/s12951-025-03382-2.

Supplementary Material 1: Identification of ACE-II Cell Purity by Immunofluorescence Staining.

Supplementary Material 2: Spectra of Different Materials. Note: (A) FT-IR spectra of βCD, MCD, and PCD. (B) 1H NMR spectrum of βCD in DMSO-d6. (C) 1H NMR spectrum of MCD in DMSO-d6. (D) 1H NMR spectrum of PCD in CD3OD. (E-G) The hydrolysis curves of MCD NPs (E), PCD NPs (F), and DCD NPs (G) in PBS solutions at pH 5, pH 6, or pH 7.4 (with or without 1 mM H2O2).

Supplementary Material 3: In Vitro Cytotoxicity and In Vivo Biodistribution of NPs. Note: (A-B) Effects of different concentrations of GDF15-GNPs (A) and GNPs$^{anti-SP-C}$ (B) on MLE12 cell viability after 24h of incubation, as measured by CCK-8 assay. * indicates $p < 0.05$ compared to control (0 μM), ** indicates $p < 0.01$ compared to control (0 μM); (C) Representative IVIS images of various isolated organs from mice treated with saline, Cy5/GNPs, or Cy5/GNPs$^{anti-SP-C}$ for 2 days, $n = 3$. Cell experiments were repeated three times.

Supplementary Material 4: Figure S4. H%E Staining of Major Organs (excluding lungs) in ALI Mice from Different Groups.Note: Scale bars = 100 μm.

Supplementary Material 5: Figure S5. Quality Control, Filtering, and Principal Component Analysis of scRNA-seq Data. Note: (A) Violin plots showing the number of genes per cell (nFeature_RNA), number of mRNA molecules per cell (nCount_RNA), and the percentage of mitochondrial genes (percent.mt) in scRNA-seq data; (B) Scatter plots displaying the correlation between nCount_RNA and percent.mt, as well as between nCount_RNA and nFeature_RNA after filtering; (C) Variance analysis identifying highly variable genes, with red representing the top 2000 highly variable genes and black representing low variability genes. The names of the top 10 highly variable genes are labeled; (D) Cell cycle states of each cell in

the scRNA-seq data, with S.Score indicating the S phase and G2M.Score indicating the G2/M phase; (E) Heatmap of the top 20 PC genes from PC_1 to PC_6 in PCA, where yellow indicates upregulated expression and purple indicates downregulated expression; (F) Distribution of cells in PC_1 and PC_2 before batch correction, with each point representing a single cell.

Supplementary Material 6: Figure S6. Cellular Clustering of scRNA-seq Data. Note: (A) Diagram illustrating the batch correction process using Harmony, with the horizontal axis representing the number of interaction rounds. (B) Distribution of cells in PC_1 and PC_2 after Harmony batch correction, with each point representing a cell. (C) Distribution of standard deviations for PCs, where important PCs exhibit larger standard deviations. (D) Visualization of clustering results via UMAP, depicting the aggregation and distribution of cells, with each color representing a specific cluster. (E) Two-dimensional UMAP visualization of clustering results, showcasing the aggregation and distribution of cells from the untreated and treated groups, where blue represents the treated group and green represents the untreated group

Supplementary Material 7: Figure S7. UMAP Clustering Tree of scRNA-seq Data. Note: Clustering at different resolutions displayed using the Clustree package.

Supplementary Material 8: Figure S8. Regulation of AMPK/SIRT1 Signaling Pathway Proteins and Cellular Senescence Factors in NPs-treated LPS-induced MLE12 Cells. Note: (A) LDH activity detection in MLE12 cell groups; (B-C) ELISA measurement of IL-β (B) and IL-6 (C) levels in cell supernatants; (D) Western blot analysis of GDF15 and AMPK/SIRT1 signaling pathway proteins in MLE12 cell groups; (E-G) statistical analysis of GDF15 (E), SIRT1 (F) protein expression, and p-AMPK/AMPK ratio (G); (H) Detection of cellular senescence in MLE12 cell groups using SA-β-Gal staining, with scale bars set at 50 μ-; (I-L) RT-qPCR analysis of mRNA expression of senescence-related factors Cdkn2a (I), Cdkn1a (J), IL-8 (K), and Mmp9 (L). (M) JC-1 staining to assess mitochondrial membrane potential in different groups. JC-1 aggregates (red) indicate normal mitochondrial membrane potential, while JC-1 monomers (green) indicate depolarized mitochondrial membrane potential. (N) Cell cycle analysis in different groups. Cell experiments were repeated thrice, * indicates $p < 0.05$ compared to the Control group, # indicates $p < 0.05$ compared to the LPS group, % indicates $p < 0.05$ compared to the GNPs group.

Supplementary Material 9: Figure S9. The Effect of GNPsanti-SP-C in Regulating the AMPK/SIRT1 Pathway on Cellular Senescence in MLE12 Cells. Note: (A) Western blot analysis of AMPK/SIRT1 signaling pathway protein expression in each group of MLE12 cells; (B-C) Protein expression of SIRT1 (B) and statistical analysis of p-AMPK/AMPK ratio (C) in each group; (D) LDH activity assay in each group of MLE12 cells; (E) ELISA assessment of IL-1μ and IL-6 levels in the cell culture supernatants of each group; (F) Senescence evaluation in each group of MLE12 cells through SA-μ-Gal staining, with Scale bars set at 50 μm; (G) RT-qPCR analysis of mRNA expression of senescence-related factors in each group; (H-I) Western blot analysis of mitochondrial and nuclear protein expression in each group of MLE12 cells, including statistical analysis of the MTCO1/ATP5A ratio; (J-K) Western blot assessment of UPRmt-related protein expression in each group of MLE12 cells. Cell experiments were conducted in triplicate, * indicates $p < 0.05$ compared to the LPS group, # indicates $p < 0.05$ compared to the GNPsanti-SP-C group.

Supplementary Material 10: Figure S10. Impact of $GNPs^{anti-SP-C}$ on ALI Mouse Lung Injury through the Regulation of the AMPK/SIRT1 Pathway. Note: (A) Histopathological changes in mouse lung tissues were examined by H&E staining, Scale bars = 50μm; (B) LDH activity in mouse BALF of each group; (C) Lung wet-to-dry weight ratio in each group of mice; (D) Total protein concentration in BALF of each group of mice; (E-G) Evaluation of lung function in each group of mice through airway resistance (E), lung compliance (F), and lung ventilation (G); (H-J) Arterial blood gas analyzer detection of $PaO_2$ (H), $PaCO_2$ (I), and $TCO_2$ (J); (K-L) ELISA measurement of pro-inflammatory cytokines IL-1β (K) and IL-6 (L) levels in BALF of each group of mice; (M) Total cell count in BALF of each group of mice; (N) ELISA measurement of MPO activity in lung tissues of each group of mice. * indicates $\boldsymbol{p} < 0.05$ compared to the Model group, # indicates $\boldsymbol{p} < 0.05$ compared to the $GNPs^{anti-SP-C}$ group, with 6 mice in each group

Supplementary Material 11

**Acknowledgements**
Not applicable.

**Author contributions**
L.G. and F.Z. contributed equally to this work. L.G. and F.Z. designed and performed the experiments, analyzed the data, and wrote the manuscript. Z.F. and W.W. supervised the study, provided conceptual guidance, and critically revised the manuscript. L.G. conducted the in vivo experiments, including the LPS-induced ALI mouse model and histopathological analysis. F.Z. was responsible for nanoparticle synthesis, characterization, and in vitro studies. Z.F. and W.W. contributed to single-cell transcriptomic and proteomic analyses and provided essential reagents and materials. All authors reviewed and approved the final manuscript.

**Funding**
This work was supported by the High-Quality Development Projects of China Medical University, supported by the Science and Technology Bureau of Liaoning Province (Grant Number: 2023JH2/20200121).

**Data availability**
Data availabilityAll data generated or analyzed during this study are included in this article and/or its supplementary material files. Further enquiries can be directed to the corresponding author.

## Declarations

**Ethics approval and consent to participate**
All animal experiments were approved by the Animal Ethics Committee of Shengjing Hospital of China Medical University (No. CMUKT20241855).

**Competing interests**
The authors declare no competing interests.

**Author details**
[1]Department of Critical Care Medicine, Shengjing Hospital of China Medical University, Shenyang, Liaoning, China
[2]Department of Thoracic Surgery, Shengjing Hospital of China Medical University, Shenyang, Liaoning, China
[3]Department of Anesthesiology, Shengjing Hospital of China Medical University, 36 Sanhao Street, Heping District, Shenyang, Liaoning Province, China

Received: 5 December 2024 / Accepted: 10 April 2025
Published online: 08 May 2025

**References**

1. Hu Q, Zhang S, Yang Y, Yao J-Q, Tang W-F, Lyon CJ et al. Extracellular vesicles in the pathogenesis and treatment of acute lung injury [Internet]. Military Med Res. Springer Science and Business Media LLC; 2022 [cited 2025 Mar 19]. Available from: https://doi.org/10.1186/s40779-022-00417-9
2. Scozzi D, Liao F, Krupnick AS, Kreisel D, Gelman AE. The role of neutrophil extracellular traps in acute lung injury [Internet]. Front. Immunol. Frontiers Media SA; 2022 [cited 2025 Mar 19]. Available from: https://doi.org/10.3389/fimmu.2022.953195
3. Li J, Deng S, Li J, Li L, Zhang F, Zou Y et al. Obacunone alleviates ferroptosis during lipopolysaccharide-induced acute lung injury by upregulating Nrf2-dependent antioxidant responses [Internet]. Cell Mol Biol Lett. Springer Science and Business Media LLC; 2022 [cited 2025 Mar 19]. Available from: https://doi.org/10.1186/s11658-022-00318-8
4. Aubron C, Hourmant B, Menguy J, Sparrow RL. Transfusion-related respiratory complications in intensive care: A diagnosis challenge [Internet]. Transfusion Clinique et Biologique. Elsevier BV; 2021 [cited 2025 Mar 19]. pp. 344–8. Available from: https://doi.org/10.1016/j.tracli.2021.09.007
5. Kemeç Z, Akgül F. Relationship between Acute Kidney Injury Requiring Renal Replacement Treatment and Mortality in Patients with Covid-19 [Internet]. Nigerian Journal of Clinical Practice. Medknow; 2022 [cited 2025 Mar 19]. pp. 1348–56. Available from: https://doi.org/10.4103/njcp.njcp_290_22
6. Ackfeld T, Schmutz T, Guechi Y, Le Terrier C. Blood Transfusion Reactions—A Comprehensive Review of the Literature including a Swiss Perspective

[Internet]. JCM. MDPI AG; 2022 [cited 2025 Mar 19]. p. 2859. Available from: https://doi.org/10.3390/jcm11102859
7. Graham CA, DuBois D, Gleason C, Kumagai J, Sanford J. Identifying and Understanding Transfusion Reactions in the Oncology Population [Internet]. Seminars in Oncology Nursing. Elsevier BV; 2021 [cited 2025 Mar 19]. p. 151137. Available from: https://doi.org/10.1016/j.soncn.2021.151137
8. Long ME, Mallampalli RK, Horowitz JC. Pathogenesis of pneumonia and acute lung injury [Internet]. Clinical Science. Portland Press Ltd.; 2022 [cited 2025 Mar 19]. pp. 747–69. Available from: https://doi.org/10.1042/cs20210879
9. Yu Y, Lian Z. Update on transfusion-related acute lung injury: an overview of its pathogenesis and management [Internet]. Front. Immunol. Frontiers Media SA; 2023 [cited 2025 Mar 19]. Available from: https://doi.org/10.3389/fimmu.2023.1175387
10. Siddiqui JA, Pothuraju R, Khan P, Sharma G, Muniyan S, Seshacharyulu P, Pathophysiological role of growth differentiation factor 15 (GDF15) in obesity, cancer, and cachexia [Internet]. CytokineGrowth Factor Reviews., Elsevier BV et al. 2022 [cited 2025 Mar 19]. pp. 71–83. Available from: https://doi.org/10.1016/j.cytogfr.2021.11.002
11. Wang D, Day EA, Townsend LK, Djordjevic D, Jørgensen SB, Steinberg GR. GDF15: emerging biology and therapeutic applications for obesity and cardiometabolic disease [Internet]. Nat Rev Endocrinol. Springer Science and Business, Media LLC. 2021 [cited 2025 Mar 19]. pp. 592–607. Available from: https://doi.org/10.1038/s41574-021-00529-7
12. Keipert S, Ost M. Stress-induced FGF21 and GDF15 in obesity and obesity resistance [Internet]. Trends in Endocrinology & Metabolism. Elsevier BV; 2021 [cited 2025 Mar 19]. pp. 904–15. Available from: https://doi.org/10.1016/j.tem.2021.08.008
13. Zhang C, Vincelette LK, Reimann F, Liberles SD. A brainstem circuit for nausea suppression [Internet]. Cell Reports. Elsevier BV; 2022 [cited 2025 Mar 19]. p. 110953. Available from: https://doi.org/10.1016/j.celrep.2022.110953
14. Wang Y, Chen C, Chen J, Sang T, Peng H, Lin X et al. Overexpression of NAG-1/GDF15 prevents hepatic steatosis through inhibiting oxidative stress-mediated dsDNA release and AIM2 inflammasome activation [Internet]. Redox Biology. Elsevier BV; 2022 [cited 2025 Mar 19]. p. 102322. Available from: https://doi.org/10.1016/j.redox.2022.102322
15. Li X, Huai Q, Zhu C, Zhang X, Xu W, Dai H, GDF15 Ameliorates Liver Fibrosis by Metabolic Reprogramming of Macrophages to Acquire Anti-Inflammatory Properties [Internet]., Cellular, Gastroenterology M, Elsevier H et al. BV; 2023 [cited 2025 Mar 19]. pp. 711–34. Available from: https://doi.org/10.1016/j.jcmgh.2023.07.009
16. Tsai C-F, Chen Y-C, Li Y-Z, Wu C-T, Chang P-C, Yeh W-L. Imperatorin ameliorates pulmonary fibrosis via GDF15 expression [Internet]. Front. Pharmacol. Frontiers Media SA; 2023 [cited 2025 Mar 19]. Available from: https://doi.org/10.3389/fphar.2023.1292137
17. Babalghith AO, Al-kuraishy HM, Al-Gareeb AI, De Waard M, Sabatier J-M, Saad HM et al. The Potential Role of Growth Differentiation Factor 15 in COVID-19: A Corollary Subjective Effect or Not? [Internet]. Diagnostics. MDPI AG; 2022 [cited 2025 Mar 19]. p. 2051. Available from: https://doi.org/10.3390/diagnostics12092051
18. Ha G, De Torres F, Arouche N, Benzoubir N, Ferratge S, Hatem E et al. GDF15 secreted by senescent endothelial cells improves vascular progenitor cell functions [Internet]. PLoS ONE. Public Library of Science (PLoS); 2019 [cited 2025 Mar 19]. p. e0216602. Available from: https://doi.org/10.1371/journal.pone.0216602
19. Shah FA, Bahudhanapati H, Jiang M, Tabary M, van der Geest R, Tolman NJ et al. Lung Epithelium Releases Growth Differentiation Factor 15 in Response to Pathogen-mediated Injury [Internet]. Am J Respir Cell Mol Biol. American Thoracic Society; 2024 [cited 2025 Mar 19]. pp. 379–91. Available from: https://doi.org/10.1165/rcmb.2023-0429oc
20. Sadek MA, Rabie MA, El Sayed NS, Sayed HM, Kandil EA. Neuroprotective effect of curcumin against experimental autoimmune encephalomyelitis-induced cognitive and physical impairments in mice: an insight into the role of the AMPK/SIRT1 pathway [Internet]. Inflammopharmacol. Springer Science and Business Media LLC; 2023 [cited 2025 Mar 19]. pp. 1499–518. Available from: https://doi.org/10.1007/s10787-023-01399-3
21. Li Q, Tan J-X, He Y, Bai F, Li S-W, Hou Y-W et al. Atractylenolide III ameliorates Non-Alcoholic Fatty Liver Disease by activating Hepatic Adiponectin Receptor 1-Mediated AMPK Pathway [Internet]. Int. J. Biol. Sci. Ivyspring International Publisher; 2022 [cited 2025 Mar 19]. pp. 1594–611. Available from: https://doi.org/10.7150/ijbs.68873
22. Xu C, Song Y, Wang Z, Jiang J, Piao Y, Li L, et al. Pterostilbene suppresses oxidative stress and allergic airway inflammation through AMPK/Sirt1 and Nrf2/HO-1 pathway s[Internet]. Immunity Inflam & Disease. Wiley; 2021 [cited 2025 Mar 19]. 1406–17.Available from: https://doi.org/10.1002/iid3.490.
23. Xu Y, Yu T, Ma G, Zheng L, Jiang X, Yang F et al. Berberine modulates deacetylation of PPARγ to promote adipose tissue remodeling and thermogenesis via AMPK/SIRT1 pathway [Internet]. Int. J. Biol. Sci. Ivyspring International Publisher; 2021 [cited 2025 Mar 19]. pp. 3173–87. Available from: https://doi.org/10.7150/ijbs.62556
24. Taouktsi E, Kyriakou E, Voulgaraki E, Verganelakis D, Krokou S, Rigas S et al. Mitochondrial p38 Mitogen-Activated Protein Kinase: Insights into Its Regulation of and Role in LONP1-Deficient Nematodes [Internet]. IJMS. MDPI AG; 2023 [cited 2025 Mar 19]. p. 17209. Available from: https://doi.org/10.3390/ijms242417209
25. Yildirim AD, Citir M, Dogan AE, Veli Z, Yildirim Z, Tufanli O et al. ER Stress-Induced Sphingosine-1-Phosphate Lyase Phosphorylation Potentiates the Mitochondrial Unfolded Protein Response [Internet]. Journal of Lipid Research. Elsevier BV; 2022 [cited 2025 Mar 19]. p. 100279. Available from: https://doi.org/10.1016/j.jlr.2022.100279
26. Xia L, Zhang C, Lv N, Liang Z, Ma T, Cheng H et al. AdMSC-derived exosomes alleviate acute lung injury via transferring mitochondrial component to improve homeostasis of alveolar macrophages [Internet]. Theranostics. Ivyspring International Publisher; 2022 [cited 2025 Mar 19]. pp. 2928–47. Available from: https://doi.org/10.7150/thno.69533
27. Li J, Lu K, Sun F, Tan S, Zhang X, Sheng W et al. Panaxydol attenuates ferroptosis against LPS-induced acute lung injury in mice by Keap1-Nrf2/HO-1 pathway [Internet]. J Transl Med. Springer Science and Business Media LLC; 2021 [cited 2025 Mar 19]. Available from: https://doi.org/10.1186/s12967-021-02745-1
28. Zhang Z, Xie K, Luo R, Zhang D, He Z, Li K et al. Dexmedetomidine alleviates acute lung injury by promoting Tregs differentiation via activation of AMPK/SIRT1 pathway [Internet]. Inflammopharmacol. Springer Science and Business Media LLC; 2022 [cited 2025 Mar 19]. pp. 423–38. Available from: https://doi.org/10.1007/s10787-022-01117-5
29. He S, Jiang X, Yang J, Wu Y, Shi J, Wu X et al. Nicotinamide mononucleotide alleviates endotoxin-induced acute lung injury by modulating macrophage polarization via the SIRT1/NF-κB pathway [Internet]. Pharmaceutical Biology. Informa UK Limited; 2023 [cited 2025 Mar 19]. pp. 22–32. Available from: https://doi.org/10.1080/13880209.2023.2292256
30. Saito S, Furuno A, Sakurai J, Park H-R, Shin-ya K, Tomida A, Compound C. Prevents the Unfolded Protein Response during Glucose Deprivation through a Mechanism Independent of AMPK and BMP Signaling [Internet]. PLoS ONE. Public Library of Science (PLoS); 2012 [cited 2025 Mar 19]. p. e45845. Available from: https://doi.org/10.1371/journal.pone.0045845
31. Broussy S, Laaroussi H, Vidal M. Biochemical mechanism and biological effects of the inhibition of silent information regulator 1 (SIRT1) by EX-527 (SEN0014196 or selisistat) [Internet]. Journal of Enzyme Inhibition and Medicinal Chemistry. Informa UK Limited; 2020 [cited 2025 Mar 19]. pp. 1124–36. Available from: https://doi.org/10.1080/14756366.2020.1758691
32. Jahan S, Ansari UA, Siddiqui AJ, Iqbal D, Khan J, Banawas S et al. Nobiletin Ameliorates Cellular Damage and Stress Response and Restores Neuronal Identity Altered by Sodium Arsenate Exposure in Human iPSCs-Derived hNPCs [Internet]. Pharmaceuticals. MDPI AG; 2022 [cited 2025 Mar 19]. p. 593. Available from: https://doi.org/10.3390/ph15050593
33. Xu N, Ren Y, Bao Y, Shen X, Kang J, Wang N et al. PUF60 promotes cell cycle and lung cancer progression by regulating alternative splicing of CDC25C [Internet]. Cell Reports. Elsevier BV; 2023 [cited 2025 Mar 19]. p. 113041. Available from: https://doi.org/10.1016/j.celrep.2023.113041
34. Song H, Chen Q, Xie S, Huang J, Kang G. GDF-15 prevents lipopolysaccharide-mediated acute lung injury via upregulating SIRT1 [Internet]. Biochemical and Biophysical Research Communications., Elsevier BV. 2020 [cited 2025 Mar 19]. pp. 439–46. Available from: https://doi.org/10.1016/j.bbrc.2020.03.103
35. Deng M, Su D, Xiao N, Zhang Z, Wang Y, Zong F et al. Gdf15 deletion exacerbates acute lung injuries induced by intratracheal inoculation of aerosolized ricin in mice [Internet]. Toxicology. Elsevier BV; 2022 [cited 2025 Mar 19]. p. 153135. Available from: https://doi.org/10.1016/j.tox.2022.153135
36. St. Sauver JL, Weston SA, Atkinson EJ, Mc Gree ME, Mielke MM, White TA et al. Biomarkers of cellular senescence and risk of death in humans [Internet]. Aging Cell. Wiley; 2023 [cited 2025 Mar 19]. Available from: https://doi.org/10.1111/acel.14006
37. Aguilar-Recarte D, Barroso E, Gumà A, Pizarro-Delgado J, Peña L, Ruart M et al. GDF15 mediates the metabolic effects of PPARβ/δ by activating AMPK [Internet]. Cell Reports. Elsevier BV; 2021 [cited 2025 Mar 19]. p. 109501. Available from: https://doi.org/10.1016/j.celrep.2021.109501

38. Cordeiro AV, Brícola RS, Braga RR, Lenhare L, Silva VRR, Anaruma CP et al. Aerobic Exercise Training Induces the Mitonuclear Imbalance and UPRmt in the Skeletal Muscle of Aged Mice [Internet]. The Journals of Gerontology: Series A. Oxford University Press (OUP); 2020 [cited 2025 Mar 19]. pp. 2258–61. Available from: https://doi.org/10.1093/gerona/glaa059
39. Mouchiroud L, Houtkooper RH, Moullan N, Katsyuba E, Ryu D, Cantó C et al. The NAD+/Sirtuin Pathway Modulates Longevity through Activation of Mitochondrial UPR and FOXO Signaling [Internet]. Cell. Elsevier BV; 2013 [cited 2025 Mar 19]. pp. 430–41. Available from: https://doi.org/10.1016/j.cell.2013.06.016
40. Shi L, Tan Y, Zheng W, Cao G, Zhou H, Li P, CTRP3 alleviates mitochondrial dysfunction and oxidative stress injury in pathological cardiac hypertrophy by activating UPRmt via the SIRT1/ATF5 axis [Internet]. Cell Death Discov. Springer Science and Business, Media LLC et al. 2024 [cited 2025 Mar 19]. Available from: https://doi.org/10.1038/s41420-024-01813-x
41. Sharma R, Reinstadler B, Engelstad K, Skinner OS, Stackowitz E, Haller RG et al. Circulating markers of NADH-reductive stress correlate with mitochondrial disease severity [Internet]. Journal of Clinical Investigation. American Society for Clinical Investigation; 2021 [cited 2025 Mar 19]. Available from: https://doi.org/10.1172/jci136055
42. Kato ET, Morrow DA, Guo J, Berg DD, Blazing MA, Bohula EA et al. Growth differentiation factor 15 and cardiovascular risk: individual patient meta-analysis [Internet]. European Heart Journal. Oxford University Press (OUP); 2022 [cited 2025 Mar 19]. pp. 293–300. Available from: https://doi.org/10.1093/eurheartj/ehac577
43. Eltokhy AK, Khattab HA, Rabah HM. The impact of cichorium intybus L. On GDF-15 level in obese diabetic albino mice as compared with metformin effect [Internet]. J Diabetes Metab Disord. Springer Science and Business Media LLC; 2021 [cited 2025 Mar 19]. pp. 1119–28. Available from: https://doi.org/10.1007/s40200-021-00828-w
44. Sarkar S, Melchior JT, Henry HR, Syed F, Mirmira RG, Nakayasu ES et al. GDF15: a potential therapeutic target for type 1 diabetes [Internet]. Expert Opinion on Therapeutic Targets. Informa UK Limited; 2022 [cited 2025 Mar 19]. pp. 57–67. Available from: https://doi.org/10.1080/14728222.2022.2029410
45. Fung E, Kang L, Sapashnik D, Benard S, Sievers A, Liu Y et al. Fc-GDF15 glycoengineering and receptor binding affinity optimization for body weight regulation [Internet]. Sci Rep. Springer Science and Business Media LLC; 2021 [cited 2025 Mar 19]. Available from: https://doi.org/10.1038/s41598-021-87959-5
46. Bhalani DV, Nutan B, Kumar A, Singh Chandel AK. Bioavailability Enhancement Techniques for Poorly Aqueous Soluble Drugs and Therapeutics [Internet]. Biomedicines. MDPI AG; 2022 [cited 2025 Mar 19]. p. 2055. Available from: https://doi.org/10.3390/biomedicines10092055
47. Bhattacharya S, Prajapati BG, Singh S, Anjum MM. Nanoparticles drug delivery for 5-aminolevulinic acid (5-ALA) in photodynamic therapy (PDT) for multiple cancer treatment: a critical review on biosynthesis, detection, and therapeutic applications [Internet]. J Cancer Res Clin Oncol. Springer Science and Business Media LLC; 2023 [cited 2025 Mar 19]. pp. 17607–34. Available from: https://doi.org/10.1007/s00432-023-05429-z
48. Yazdian-Robati R, Bayat P, Dehestani S, Hashemi M, Taghdisi SM, Abnous K. Smart delivery of epirubicin to cancer cells using aptamer-modified ferritin nanoparticles [Internet]. Journal of Drug Targeting. Informa UK Limited; 2022 [cited 2025 Mar 19]. pp. 567–76. Available from: https://doi.org/10.1080/1061186x.2022.2025600
49. Gebert M, Sławski J, Kalinowski L, Collawn JF, Bartoszewski R. The Unfolded Protein Response: A Double-Edged Sword for Brain Health [Internet]. Antioxidants. MDPI AG; 2023 [cited 2025 Mar 19]. p. 1648. Available from: https://doi.org/10.3390/antiox12081648
50. Li J, Zhang D, Zhang Y, Ge J, Yang C. Mitochondria-specific antioxidant Mito-TEMPO alleviates senescence of bone marrow mesenchymal stem cells in ovariectomized rats [Internet]. Journal Cellular Physiology. Wiley; 2024 [cited 2025 Mar 19]. Available from: https://doi.org/10.1002/jcp.31323
51. Inigo JR, Chandra D. The mitochondrial unfolded protein response (UPRmt): shielding against toxicity to mitochondria in cancer [Internet]. J Hematol Oncol. Springer Science and Business, Media LLC. 2022 [cited 2025 Mar 19]. Available from: https://doi.org/10.1186/s13045-022-01317-0
52. Eckl E-M, Ziegemann O, Krumwiede L, Fessler E, Jae LT. Sensing, signaling and surviving mitochondrial stress [Internet]. Cell. Mol. Life Sci. Springer Science and Business Media LLC; 2021 [cited 2025 Mar 19]. pp. 5925–51. Available from: https://doi.org/10.1007/s00018-021-03887-7


## Publisher's note